# Transcription processes compete with loop extrusion to homogenize promoter and enhancer dynamics

Angeliki Platania, Cathie Erb, Mariano Barbieri, Bastien Molcrette, Erwan Grandgirard, Marit de Kort, Wim Pomp, Karen Meaburn, Tiegh Taylor, Virlana Shchuka, et al.

GENETICS

# Transcription processes compete with loop extrusion to homogenize promoter and enhancer dynamics

**Angeliki Platania[1], Cathie Erb[1], Mariano Barbieri[2], Bastien Molcrette[1], Erwan Grandgirard[1], Marit A. C. de Kort[3], Wim Pomp[3], Karen Meaburn[4], Tiegh Taylor[5], Virlana M. Shchuka[5], Silvia Kocanova[6], Mariia Nazarova[1], Guilherme Monteiro Oliveira[1], Jennifer A. Mitchell[5], Evi Soutoglou[4], Tineke L. Lenstra[3], Nacho Molina[1], Argyris Papantonis[2], Kerstin Bystricky[6,7], Tom Sexton[1]***



**The spatiotemporal configuration of genes with distal regulatory elements is believed to be crucial for transcriptional control, but full mechanistic understanding is lacking. We combine simultaneous live tracking of pairs of genomic loci and nascent transcripts with molecular dynamics simulations to assess the *Sox2* gene and its enhancer. We find that both loci exhibit more constrained mobility than control sequences due to stalled cohesin at CCCTC-binding factor sites. Strikingly, enhancer mobility becomes constrained on transcriptional firing, homogenizing its dynamics with the gene promoter, suggestive of their cotranscriptional sharing of a nuclear microenvironment. Furthermore, we find transcription and loop extrusion to be antagonistic processes constraining regulatory loci. These findings indicate that modulating chromatin mobility can be an additional, underestimated means for effective gene regulation.**

## INTRODUCTION

Metazoan gene expression is finely controlled by regulatory inputs from promoter sequences and distal regulatory elements, such as enhancers. How these dispersed elements are spatiotemporally coordinated to determine transcriptional output has been a topic of intense study, but key questions remain unresolved. (*1*, *2*). An often-overlooked aspect determining how regulatory chromatin architectures are built or maintained is the underlying mobility (and freedom of movement) of the component factors. Whereas nonhistone chromatin proteins, including transcription factors, are highly mobile in the nucleoplasm (*3*), the large polymeric chromatin fiber has more constrained movement due to a crowded environment and elastic interactions with neighboring segments of the polymer (*4*). This is often characterized as subdiffusive movement, whereby the mean squared displacement (MSD) of the genomic element follows the relationship with time, *t*: $MSD \propto D_\alpha t^\alpha$, where $D_\alpha$ is the diffusion coefficient (a proxy for diffusive speed), and α, the anomalous exponent, is smaller than the value of 1 found in classical Brownian diffusion. We previously showed that an estrogen-inducible transgene explored a much smaller nuclear volume on acute induction and that this constraint was dependent on transcription initiation (*5*). This is supported by analogous studies showing slowed movement of the pluripotency gene *Nanog* when transcriptionally active (*6*) and global enhanced chromatin mobility on treatment with transcriptional inhibitors (*7*, *8*). However, mobility of the *Oct4* gene was found to be insensitive to transcriptional status (*6*), and comparison of promoter and enhancer motion between embryonic stem cells (ESCs) and epiblast-like cells reported both sequences' dynamics to be greater in the cell state where the elements are active (*9*). Few of these prior studies directly visualized transcripts, so only indirect conclusions relative to gene expression were able to be drawn. At a larger scale, promoter-enhancer communication takes place within the context of topologically associated domains (TADs), regions of preferential intra-domain chromatin contacts identified in population-average Hi-C maps (*10*, *11*). The major mechanism believed to shape TADs is loop extrusion by SMC protein complexes, particularly cohesin (*12*). Loop extrusion is stalled on interaction with CCCTC-binding factor (CTCF)–bound sites, providing the basis for loop formation at TAD borders (*13*). However, recent live imaging experiments have revealed these to be relatively rare and transient interactions (*14*, *15*). The so-called "architectural interactions" brought about by convergent CTCF sites have been proposed to facilitate juxtaposition of adjacent promoters and enhancers (*16*), and loop extrusion has been shown to be required for efficient gene activation by distal enhancers (*17*–*19*). Cohesin-mediated loop extrusion generally reduces chromatin mobility (*7*, *15*) perhaps further "stabilizing" such genomic configurations. However, we and others have observed extensive persistence of promoter-enhancer interactions when CTCF and/or cohesin are ablated (*20*–*22*). A clear understanding of how loop extrusion and transcriptional events modulate chromatin dynamics to regulate gene expression is thus still lacking. In this study, we simultaneously tagged the promoter, major enhancer (*Sox2* control region, SCR), and nascent transcripts of the pluripotency gene *Sox2*, in mouse ESCs, tracking their movement in response to numerous perturbations to assess more closely the interplay of enhancer activity, transcription, and cohesin-mediated loop extrusion on the spatiotemporal organization of gene regulation.

## RESULTS

### *Sox2* promoter and enhancer mobility is constrained

We labeled the *Sox2* promoter and SCR with orthologous *parS* sites (ANCHOR1 and ANCHOR3; separated by ~115 kb) in the *musculus* allele of F1 (*Mus musculus*$^{129}$ × *Mus castaneus*) hybrid ESCs (we

[1]Department of Functional Genomics and Cancer, Institute of Genetics and Molecular and Cellular Biology (IGBMC), UMR7104, Centre National de la Recherche Scientifique, U1258, Institut National de la Santé et de la Recherche Médicale, University of Strasbourg, 6704 Illkirch, France. [2]Translational Epigenetics Group, Institute of Pathology, University Medical Centre Göttingen, Göttingen, Germany. [3]Division of Gene Regulation, the Netherlands Cancer Institute, Oncode Institute, 1066CX Amsterdam, Netherlands. [4]Genome Damage and Stability Centre, School of Life Sciences, University of Sussex, Brighton, UK. [5]Department of Cell and Systems Biology, University of Toronto, Toronto, Ontario M55 3G5, Canada. [6]Molecular Cellular and Developmental Biology Unit (MCD), Centre de Biologie Integrative (CBI), University of Toulouse Paul Sabatier, CNRS, 31062 Toulouse, France. [7]Institut Universitaire de France (IUF), 75005 Paris, France.
*Corresponding author. Email: sexton@igbmc.fr

term this line *Sox2-SCR*$_{WT}$), for visualization with fluorescently labeled ParB proteins (*5*, *23*). The small size (~1 kb) of the *parS* sequences allowed us to place the tags very close to the promoter (5.5 kb upstream of the transcription start site) and inside the SCR, in between the sequences known to control *Sox2* transcription (*20*), allowing for direct imaging of both the promoter and enhancer. As a control, we also generated an ESC line (*Inter-Down*) with *parS* integration sites shifted by ~60 kb, allowing visualization of apparently nonregulatory loci of equivalent genomic separation (Fig. 1, A and B, and movies S1 and S2). Allele-specific quantitative reverse transcription polymerase chain reaction (qRT-PCR) showed that neither the integration of the *parS* sites nor their binding by transfected ParB proteins affected *Sox2* expression (fig. S1A); expression of other pluripotency markers and cell cycle progression was similarly unaffected (fig. S1, B and C). Further, allele-specific circular chromosome conformation capture-sequencing (4C-seq) showed that *Sox2*-SCR interaction strength was unaltered by *parS* integration and ParB binding (Fig. 1C), and three-dimensional (3D) DNA fluorescence in situ hybridization (FISH) measurements revealed no difference in average *Sox2*-SCR or control inter-probe distances between wild-type and *parS*-engineered ESCs (fig. S1, D and E, and data S1). Combined, these controls demonstrate that our ANCHOR imaging setup has negligible functional impact on the loci visualized in this study. We imaged the labeled loci at high temporal resolution (500 ms per frame) with spinning disk confocal microscopy. Measured *Sox2*-SCR 2D distances from these live experiments were consistently small [median, 164 nm; median absolute deviation (MAD), 56 nm], in agreement with high-resolution oligoPAINT measurements at this locus on fixed cells (median separation, 160 nm; MAD, 110 nm) (fig. S1F) (*24*). 3D DNA FISH measurements in fixed cells found the promoter and enhancer to be significantly more proximal than the control regions, as may be expected from the Hi-C map (fig. S1E). Live imaging results also showed an apparent small increase in median inter-probe distance for the control loci (187 nm; MAD, 67 nm). However, this small difference is within our estimated precision limits for inter-locus measurements in the live setup (fig. S2), which prioritizes high temporal resolution to more accurately measure locus dynamics.

Strikingly, on examination of the tracks of labeled regions around the *Sox2* locus, as well as their ensemble MSD curves, it was apparent that the promoter and enhancer were more limited in their exploration of the nuclear volume than the control regions (Fig. 1, D and E). To quantitatively assess the local chromatin motion, we applied our previously developed Gaussian processes to fractional Brownian motion (GP-FBM) method to fit the recorded trajectories to a fractional Brownian motion model and extract their apparent diffusion coefficients, $D_{\alpha\_app}$, and anomalous exponents, $\alpha_{app}$ (*25*). We confirmed that the loci motion approximated to self-similar Gaussian-distributed displacements and an FBM velocity autocorrelation function over the time scale in which measurements were taken (figs. S3 and S4), affirming the suitability of the model used. We analyzed cross-correlations of co-measured trajectories to correct for global movements of the cell/nuclear substrate (*25*). This approach was robust since the experimentally measured MSD curves fit very well to the sums of the deconvolved locus and substrate MSDs estimated by GP-FBM (fig. S5A). We stress that GP-FBM, apart from assuming proximity to a global FBM regime, is agnostic to any specific polymer model and obtains estimates of diffusive parameters for individual trajectories including those deviating from the average (Fig. 1F). Hence, the obtained values of the apparent anomalous exponent, $\alpha_{app}$, give a measure of constraint to the particle movement, which can be compared across experiments. In line with our initial observations, the average substrate-corrected apparent anomalous exponent was significantly smaller for the active elements, the *Sox2* promoter (median $\alpha_{app}$, 0.130; MAD, 0.076) and the SCR (median $\alpha_{app}$, 0.203; MAD, 0.095), than for the control regions (median $\alpha_{app}$, 0.276; MAD, 0.135 and median, 0.224; MAD, 0.108 for intervening and downstream regions, respectively), indicating a greater constraint to the local movement of the regulatory regions. In addition, the *Sox2* promoter exhibited significantly more constrained motion than the enhancer ($q = 2 \times 10^{-5}$; Wilcoxon rank sum test with Benjamini-Hochberg correction). Despite large cell-to-cell variability of diffusive parameter measurements, their distributions were consistent with single populations ($P \geq 0.36$; Hartigan dip test of unimodality). As a control, all four loci demonstrated greatly reduced mobility in fixed cells, giving measured apparent anomalous exponents close to zero (fig. S5B). We note that our measured values from live cells are comparable with those determined from fits to radial MSD curves for lac/TetO-tagged CTCF-mediated interacting sites with a similar genomic separation of ~150 kb (*15*). Analogous radial MSD analysis for the *Sox2-SCR*$_{WT}$ and *Inter-Down* trajectories confirmed similarly constrained motion, with the promoter and enhancer significantly more constrained than the control sequences [$P = 5.7 \times 10^{-6}$; analysis of covariance (ANCOVA) test; fig. S5C]. Thus, at the *Sox2* locus, the promoter and enhancer are much less free to explore the nucleus than nonregulatory elements, with the promoter displaying even less mobility than the enhancer.

## Stalled loop extrusion at CTCF sites specifically limits chromatin mobility

The *Sox2* promoter and SCR both reside at TAD boundaries in ESCs (Fig. 1A); the boundary at the enhancer is lost on differentiation to neural progenitors, whereas the one at the promoter is maintained (fig. S6A) (*26*). Since cohesin loading has been associated with generally reduced chromatin dynamics (*7*, *15*), we reasoned that stalled loop extrusion complexes at the CTCF sites of TAD borders could be a possible explanation for the specifically constrained motion of *Sox2* and the SCR. To test this hypothesis, we first assessed the mobilities of the labeled loci at the early stages of neuronal differentiation. Three days after changing the culture conditions, *Sox2* transcription is largely shut down (fig. S6B) and the interaction between *Sox2* and the SCR measured by 4C-seq is greatly reduced (fig. S6C). Concomitantly, the weaker TAD border at the SCR ($P = 0.002$; Wilcoxon rank sum test), as well as the tagged downstream locus ($P = 0.006$), had significantly increased mobility (Fig. 2, A and B). However, the stable TAD border at the *Sox2* gene retained strong mobility constraints regardless of transcriptional shutdown, with an unchanged apparent anomalous exponent ($P = 0.99$). This suggests that an aspect of the chromatin architectural organization, more than the transcriptional process itself, may be responsible for most *Sox2* gene constraints. To directly test the role of cohesin-mediated loop extrusion in constraining chromatin, we engineered a fusion of the FKBP$^{F36V}$ "degron" peptide to the C terminus of cohesin subunit RAD21 on both alleles in the *Sox2-SCR*$_{WT}$ and *Inter-Down* lines, generating *Sox2-SCR*$_{Rad21}$ and *Inter-Down*$_{Rad21}$ lines, respectively. Two hours of treatment with dTAG-13 was sufficient to degrade essentially all RAD21 protein (fig. S6D) with minimal changes to the cell cycle (fig. S6E) or *Sox2* mRNA levels (fig. S6F). Cohesin ablation caused significant relaxation (increased mobility) at the promoter,

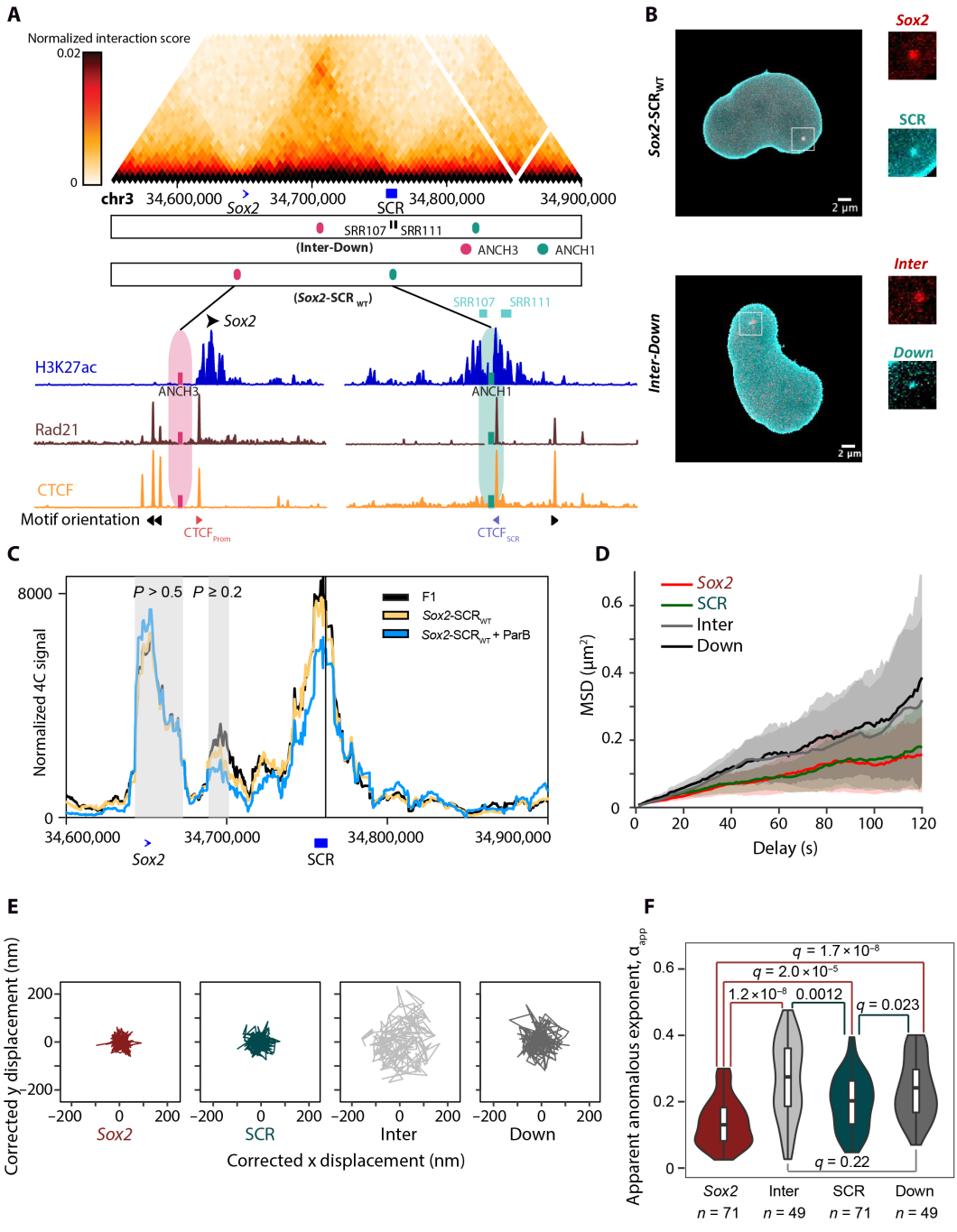


**Fig. 1. Constrained *Sox2* promoter and enhancer mobility.** (**A**) Overview of the *Sox2* locus, showing (top to bottom): ESC Hi-C map, showing the TAD delimited by *Sox2* and SCR (positions shown in blue); scaled positions of ANCH1 and ANCH3 labels inserted in the *Sox2-SCR*$_{WT}$ and *Inter-Down* ESC lines; zoomed-in ESC chromatin immunoprecipitation sequencing profiles for acetylated histone H3 lysine-27 (H3K27ac, blue), the cohesin subunit RAD21 (brown), and CTCF (orange). Red and cyan rectangles indicate the exact positions of the ANCH3 and ANCH1 labels, respectively. Positions of elements deleted in this study (SRR107 and SRR111, cyan; CTCF$_{Prom}$, red; CTCF$_{SCR}$, blue) are indicated. Orientations of major CTCF motifs are denoted by arrows. (**B**) Representative images of *Sox2-SCR*$_{WT}$ (top) and *Inter-Down* (bottom) nuclei (after segmentation and removal of cytoplasmic signal); scale bar, 2 µm. Insets show zoomed regions around spots corresponding to bound *parS* sequences. (**C**) Musculus-specific 4C-seq profiles (mean of two replicates) using the SCR as bait are shown for F1 and *Sox2-SCR*$_{WT}$ ESCs before and after transfection with ParB vectors. The two regions consistently called as interactions are denoted in gray, and the minimum *P* values for compared interaction scores with F1 (two-tailed *t* test) are denoted. (**D**) Uncorrected ensemble MSD curves for labeled *Sox2* (red), SCR (green), Inter (light gray), and Down (dark gray) sequences, with lines showing median values and shading indicating the MAD. (**E**) Sample tracks of the 2D trajectories for the same four regions as in (D), plotted on the same scale. Displacements have been corrected for substrate movement, and the plots have been centered on the median positions. (**F**) Violin plot showing the distributions of apparent anomalous exponents measured from the individual movies for each of the four regions as in (D). Comparisons are made by Wilcoxon rank sum tests with Benjamini-Hochberg multiple testing correction, with *q* values given.

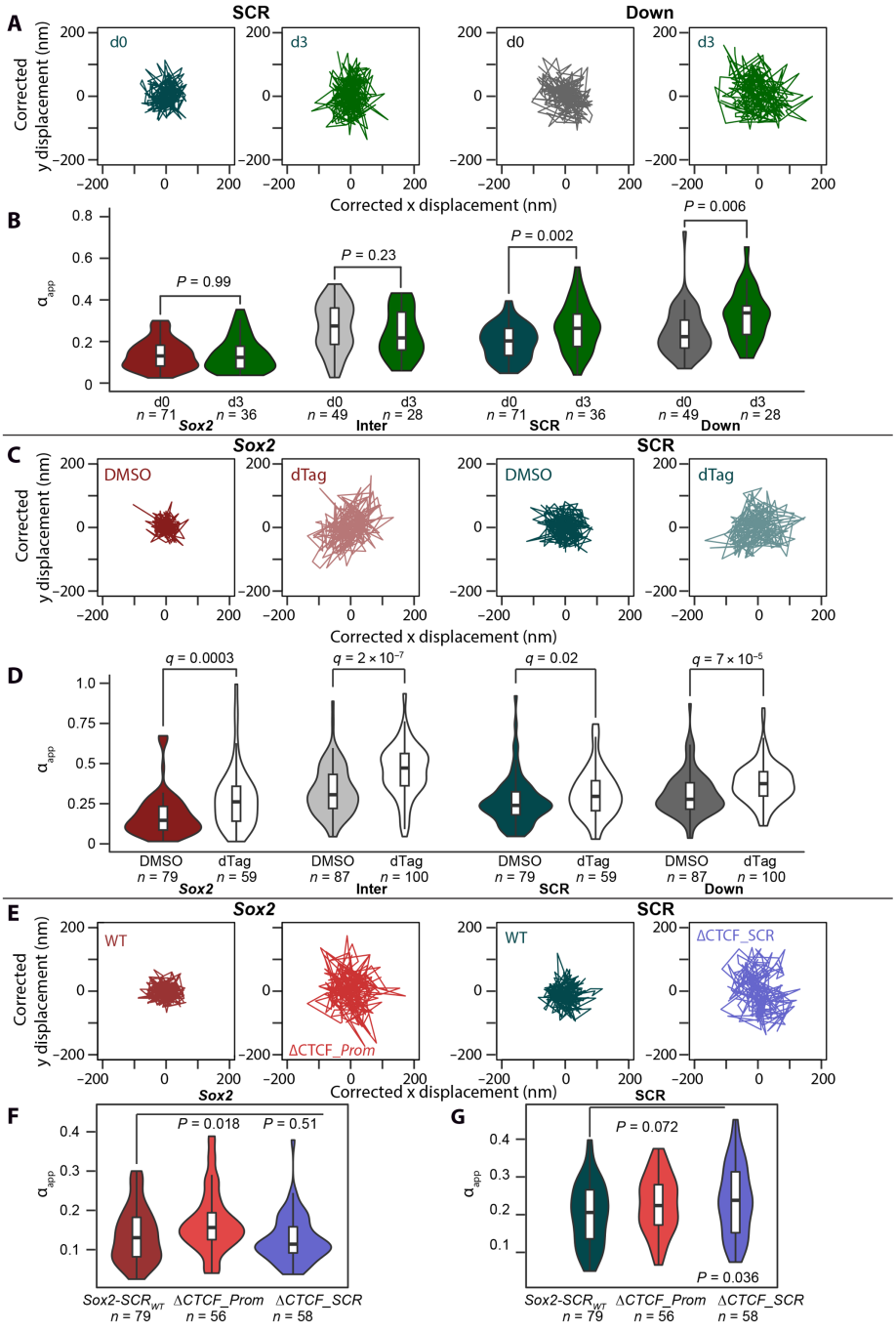


**Fig. 2. Stalled cohesin loop extrusion at CTCF sites limits chromatin mobility.** (**A**) Sample tracks of 2D trajectories for labeled SCR and Down regions, at either 0 or 3 days of differentiation, plotted on the same scale. Displacements have been corrected for substrate movement, and the plots have been centered on the median positions. (**B**) Violin plots showing the distributions of apparent anomalous exponents measured from the individual movies for *Sox2*, Inter, SCR, and Down regions, comparing 0 and 3 days of differentiation. Comparisons are made by Wilcoxon rank sum tests, with *P* values given. (**C**) Sample tracks of 2D trajectories for labeled *Sox2* and SCR regions in *Sox2-SCR*$_{Rad21}$ cells after treatment with dimethyl sulfoxide (DMSO) (control) or dTag-13 (to abrogate RAD21). Displacements have been corrected for substrate movement, and the plots have been centered on the median positions. (**D**) Violin plots showing the distributions of apparent anomalous exponents measured from the individual movies for *Sox2*, Inter, SCR, and Down regions of *Sox2-SCR*$_{Rad21}$ or *Inter-Down*$_{Rad21}$ cells, comparing DMSO and dTag-13 treatments. Comparisons are made by Wilcoxon rank sum tests with Benjamini-Hochberg correction, with *q* values given. (**E**) Sample tracks of 2D trajectories for labeled *Sox2* and SCR regions in *Sox2-SCR*$_{WT}$ cells or cells where the local CTCF site has been deleted (*Sox2-SCR*$_{\Delta CTCF\text{-}Prom}$ and *Sox2-SCR*$_{\Delta CTCF\text{-}SCR}$, respectively). Displacements have been corrected for substrate movement, and the plots have been centered on the median positions. (**F**) Violin plots showing the distributions of apparent anomalous exponents measured from the individual movies for *Sox2*, comparing *Sox2-SCR*$_{WT}$, *Sox2-SCR*$_{\Delta CTCF\text{-}Prom}$, and *Sox2-SCR*$_{\Delta CTCF\text{-}SCR}$ cells. Comparisons with wild-type are made by Wilcoxon rank sum tests, with *P* values given. (**G**) Violin plots showing the distributions of apparent anomalous exponents measured from the individual movies for SCR, comparing *Sox2-SCR*$_{WT}$, *Sox2-SCR*$_{\Delta CTCF\text{-}Prom}$, and *Sox2-SCR*$_{\Delta CTCF\text{-}SCR}$ cells. Comparisons with wild-type are made by Wilcoxon rank sum tests, with *P* values given.

enhancer, and control regions (Fig. 2, C and D; $q \leq 0.02$; Wilcoxon rank sum test with Benjamini-Hochberg correction), confirming that the complex limits locus motion generally when bound to chromatin. This could be brought about by loop extrusion processes and/or by tethering sister chromatids of cells in S-$G_2$ phase (the majority of ESCs; figs. S1C and S6E). *Sox2* and the SCR maintained significantly more constrained motion than the control regions after RAD21 ablation ($1 \times 10^{-8} \leq q \leq 0.03$; Wilcoxon rank sum test for pairwise comparisons between *Sox2*/SCR and Inter/Down regions after dTag treatment, with Benjamini-Hochberg correction). This suggests that although cohesin engagement plays a major role in generally constraining chromatin motion, other factors are also involved at promoters and enhancers.

We next assessed whether stalled loop extrusion complexes at CTCF sites could play a more localized role in constraining chromatin. We previously showed that the SCR TAD border is resilient to large genetic deletions at the enhancer, including the predominant CTCF site (*20*). To assess the role of CTCF loop anchoring on chromatin dynamics, we generated derivative lines of *Sox2-SCR*$_{WT}$ cells harboring homozygous deletions of the core CTCF-binding motifs located either just upstream of the *Sox2* promoter (*Sox2-SCR*$_{\Delta CTCF\text{-}Prom}$) or within the SCR (*Sox2-SCR*$_{\Delta CTCF\text{-}SCR}$) (Fig. 1A and fig. S7A). These deletions eliminated local CTCF binding (fig. S7B), and both lines maintained high expression of pluripotency marker genes (fig. S1B). *Sox2* expression was only mildly and nonsignificantly reduced in the *Sox2-SCR*$_{\Delta CTCF\text{-}SCR}$ line, in agreement with previous findings for homozygous deletions of this element (*27*), although expression was reduced to ~60% of wild-type levels in the *Sox2-SCR*$_{\Delta CTCF\_Prom}$ line (fig. S7C). In agreement with previous studies (*20*, *22*, *27*), deletion of the SCR CTCF site has minimal effects on chromatin architecture (as determined by allele-specific 4C-seq), and homozygous deletion of the promoter CTCF site causes only a slightly reduced interaction (fig. S7D). For both lines, the distributions of *Sox2*-SCR 2D distances were indistinguishable from *Sox2-SCR*$_{WT}$, all below the precision limits of our live imaging setup. Despite these mild phenotypic effects, local constraint on chromatin mobility was relieved when CTCF binding was abrogated: Median $\alpha_{app}$ was increased at the *Sox2* promoter in *Sox2-SCR*$_{\Delta CTCF\_Prom}$ cells ($P = 0.018$; Wilcoxon rank sum test) and at the SCR in *Sox2-SCR*$_{\Delta CTCF\_SCR}$ cells ($P = 0.036$), with negligible changes at the regulatory element which maintains CTCF binding (Fig. 2, E to G). These findings mirror the observed increase in radial MSD on deletion of CTCF-binding sites within a transgenic CTCF-mediated looping construct (*15*). However, the nature of the analysis done in this study did not distinguish whether dynamics are specifically altered locally at the CTCF anchor site or whether they are also propagated to looping anchor partners. We applied GP-FBM to the 3D trajectories from these orthogonal transgenic studies, including constructs where only one of the two CTCF sites was maintained, finding stronger chromatin constraints at the CTCF-bound site, independently of whether or not CTCF was at the distal "partner" site (fig. S7E and data S2). Collectively, these results demonstrate that stalled cohesin at CTCF sites places local constraints on chromatin mobility that are not transferred to distal CTCF sites.

## Promoter and enhancer dynamics become homogenized on transcriptional firing

Several earlier studies have suggested that transcription itself may also affect chromatin fiber motion but with seemingly conflicting results (*5*–*9*). These studies relied mostly on perturbations such as treatment with drugs or ablation of general transcription factors, which may have indirect and confounding effects. To formally assess the effect of transcription on chromatin dynamics, we generated triple-labeled ESCs (*Sox2-SCR*$_{MS2}$). We inserted MS2 repeats into the 3′ untranslated region (3′UTR) of the musculus allele of the *Sox2* gene in combination with the ANCHOR tags at the SCR and *Sox2* promoter. With subsequent PiggyBac-mediated transposition of constructs for both fluorescently-labeled ParB proteins and MS2 bacteriophage coat protein (MCP), this setup allows for the simultaneous tracking of promoter, enhancer, and nascent RNA (Fig. 3, A and B, and movie S3). Previous labeling experiments at the *Sox2* locus reported a substantial reduction in transcription and SOX2 protein levels on incorporation of the MS2/MCP system, presumably due to interference at the 3′UTR (*28*). We verified that our line, using a lower-affinity version of the MS2 repeats and with the selection marker excised, had minimal perturbation of *Sox2* expression, estimating from single-molecule RNA FISH and Western blotting to have minimal changes to transcription rates and only a mild reduction (~25%) of total protein levels in our assayed cell line (fig. S8, A to D). Imaging transcription bursts over 2-hour windows, we measured an average bursting time of 200 s and an average time between bursts of 630 s (sample traces given in fig. S8E). As a population, the observed cells spent 36% of their time with a detected burst of transcription, in line with estimates of bursting frequencies from single-molecule RNA FISH experiments in cells without the MS2 system (fig. S8D). To measure chromatin dynamics at maximum temporal resolution, we then used this line for triple-label tracking over 5-min windows. During this time frame, most cells were either always transcribing or always silent, but transition points were occasionally observed (Fig. 3B and movie S4). As for the *Sox2-SCR*$_{WT}$ line, the promoter and enhancer were frequently proximal (median 2D separation, 182 nm for transcribing alleles; MAD, 84 nm; median separation, 175 nm; MAD, 99 nm for nontranscribing alleles), and any potential differences in average distances between the two cell states could not be resolved in the live imaging setup. When comparing apparent anomalous exponents, the apparent differences we observed for promoter and enhancer mobility regimes in the double-label experiments (Fig. 1) are recapitulated only for nontranscribing alleles (fig. S8F). Strikingly, the mobility regimes of the two loci become almost indistinguishable on transcribed alleles, suggesting that their dynamics become similar on *Sox2* transcriptional firing (Fig. 3C). Moreover, the changes in dynamics of the promoter and enhancer were markedly different. The SCR displayed more constrained motion when its target gene was transcribed, with a significant reduction in its median apparent anomalous exponent ($P = 0.0078$; Wilcoxon rank sum test), reaching the equivalent level of the coupled *Sox2* promoter ($P = 0.49$; Fig. 3, D and E). Conversely, $\alpha_{app}$ of the gene promoter was insensitive to transcriptional state ($P = 0.37$), instead displaying a more generalized increase in diffusive speed (vertical shift upward on the ensemble MSD curve; Fig. 3C). We note that the promoter and enhancer dynamics of the double-labeled *Sox2-SCR*$_{WT}$ cells are equivalent to those measured in the nontranscribing alleles of *Sox2-SCR*$_{MS2}$ cells ($q = 0.75$ for *Sox2*; $q = 0.87$ for SCR; Wilcoxon rank sum test with Benjamini-Hochberg multiple testing correction; fig. S8F), fitting with our findings that most ESCs are not undergoing *Sox2* transcriptional bursts at any given time. These results unify the seemingly conflicting results of previous live imaging studies; the SCR

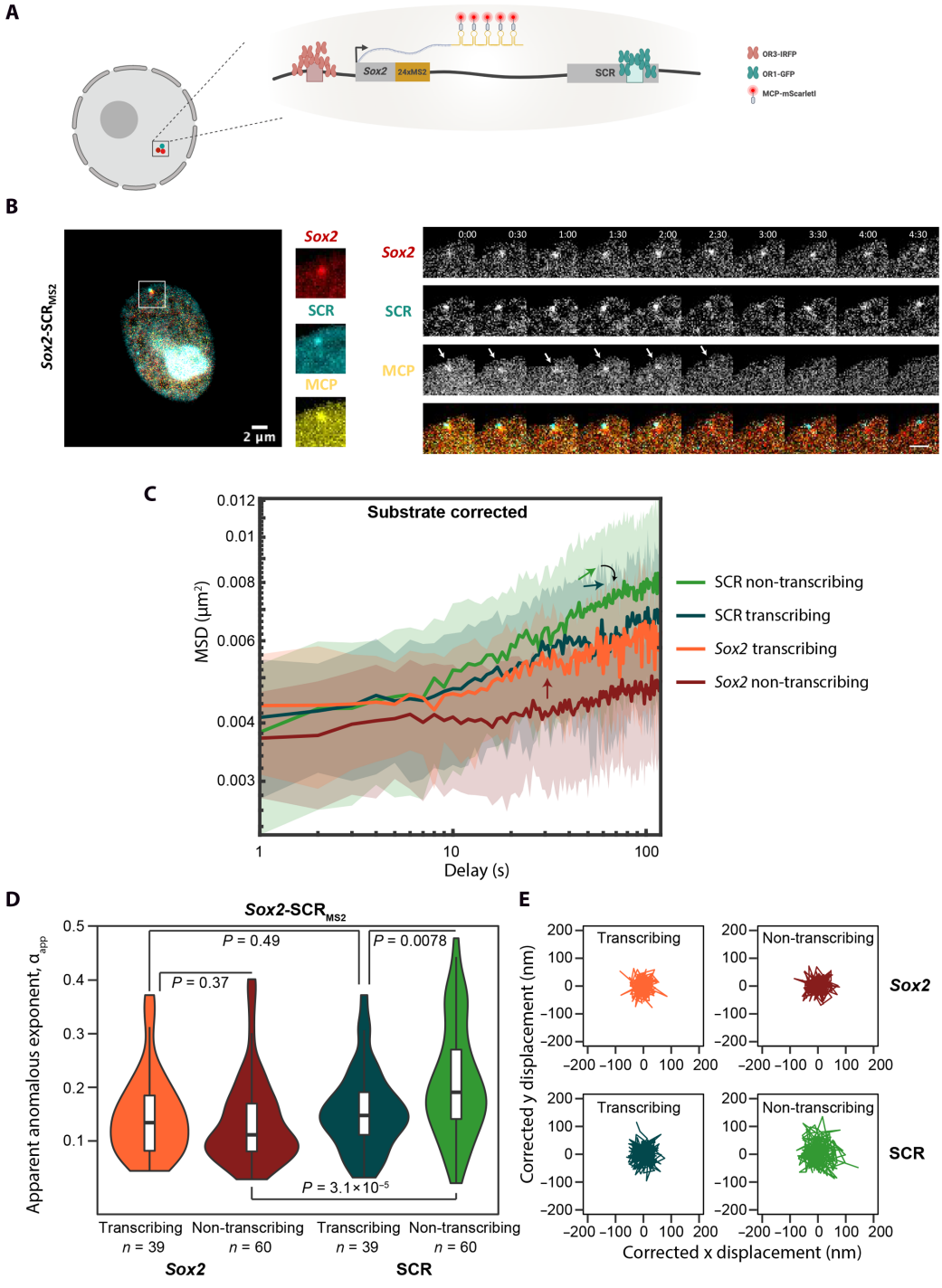


**Fig. 3. Promoter and enhancer dynamics are synchronized on transcriptional firing.** (**A**) Schematic of triple-label system of *Sox2-SCR*$_{MS2}$ ESCs. The *Sox2-SCR*$_{WT}$ line is additionally tagged with 24 copies of the MS2 repeat at *Sox2* 3′UTR for visualization of nascent RNA with MCP-ScarletI. (**B**) Left, representative image of transcriptionally active *Sox2-SCR*$_{MS2}$ nucleus, with the OR3-IRFP signal shown in red, the OR1-EGFP signal shown in cyan, and the mScarletI signal shown in yellow; scale bar, 2 μm. Insets show zoomed regions around spots corresponding to bound *parS* sequences and transcription site. Right, images of the same *Sox2-SCR*$_{MS2}$ nucleus at 30-s intervals, showing each of the three channels individually in monochrome, and the overlaid image with the same color scheme as on the left. Arrows show the position of a transcription site (MCP$^+$), which is inactivated by ~3 min. Scale bar, 2 μm. (**C**) Ensemble MSD curves, corrected for substrate movement, comparing active and inactive alleles at labeled *Sox2* (orange and dark red, respectively) and SCR (green and dark green, respectively) regions. Lines indicate median values and shading the MAD. Red arrow indicates vertical shift in MSD plot when comparing *Sox2* dynamics, and green/dark green arrows indicate the changes in slope of the SCR MSD plots. (**D**) Violin plot showing the distributions of apparent anomalous exponents measured from the individual movies for *Sox2* and SCR in *Sox2-SCR*$_{MS2}$ cells, comparing transcriptionally active and inactive alleles. Comparisons are made by Wilcoxon rank sum tests, with *P* values given. (**E**) Sample tracks of the 2D trajectories for labeled *Sox2* and SCR regions in *Sox2-SCR*$_{MS2}$ cells, which are transcriptionally active (left) or inactive (right). Displacements have been corrected for substrate movement, and the plots have been centered on the median positions.

explores a more restricted nuclear volume during transcription, in agreement with ours and others' findings at selected loci (*5*–*8*), whereas the *Sox2* promoter has increased diffusion speed (interpreted as increased $D_\alpha$, only in special cases where the anomalous exponent is unchanged), in agreement with a different study (*9*). We propose that placing constraints and altering diffusion speeds on different chromatin loci during transcription are both means to allow effective matching of enhancer dynamics with those of their target gene promoters for conferred regulation.

### Loop extrusion and transcriptional processes compete to constrain chromatin

We previously showed that deletion of a small number of transcription factor–binding sites within the SCR was sufficient to reduce *Sox2* transcription in *cis* to basal levels without affecting gene-enhancer interaction (*20*). To investigate possible effects on chromatin dynamics, we deleted the same regions (termed SRR107 and SRR111) on the *musculus* allele of *Sox2-SCR*$_{WT}$ ESCs to generate the line *Sox2-SCR*$_{\Delta SRR107+111}$ (Fig. 1A). As expected, the deletion caused drastic reduction of *Sox2* expression on the ANCHOR-labeled *cis* allele, with no effects on transcription of *Sox2* from the unlabeled allele (fig. S9A) or of other pluripotency genes (fig. S1B). On the basis of the triple-label results, we expected that SCR dynamics would either not change because of the wild-type data mostly capturing the inactive state, or would be relaxed as the transcription-coupled constraints to the enhancer are more completely removed. Unexpectedly, however, Δ*SRR107+111* caused a significant increase in movement constraint, with reduced apparent anomalous exponent ($P = 0.0048$; Wilcoxon rank sum test; Fig. 4, A and B). The $\alpha_{app}$ distribution at the *Sox2* promoter was unchanged on this deletion ($P = 0.52$), in line with our previous results demonstrating its insensitivity to transcriptional status (Fig. 3D). To try and better understand these results, we applied molecular dynamics simulations, a strategy that we recently used to predict, and then experimentally confirm, that de novo CTCF-oriented chromatin loops form when competing RNA polymerase II (Pol II) is acutely ablated (*29*). This framework was previously applied to a theoretical locus; here, we used it to model the 800-kb region around the *Sox2* locus as 2-kb beads on a chain, with the true positions of transcribed genes, enhancers, and CTCF-bound regions (see Materials and Methods). For the wild-type locus, the model successfully recapitulated the Hi-C contact map, as well as the greater mobility constraints of the *Sox2* promoter and SCR compared to control elements (fig. S9, B and C). We then modeled the *Sox2-SCR*$_{\Delta CTCF\text{-}SCR}$ line by converting the CTCF-bound bead to an unbound one, and the *Sox2-SCR*$_{\Delta SRR107,111}$ line by deleting the corresponding beads, and decreasing RNA polymerase binding at the inactivated *Sox2* promoter by 80%. Using the model parameters we had previously used (*29*) gave poor agreement with the experimental results (fig. S9D). In particular, the SCR was predicted to have increased mobility on loss of SRR107+111 and not the observed decrease. On the basis of ours and others' observations of loop extrusion and transcription as antagonistic processes (*20*–*22*, *29*–*31*), we tested models with parameters creating more competition between cohesin and polymerase chromatin occupancy (see Materials and Methods). The corresponding MSD curves for the SCR now broadly recapitulated the experimental results, with overall reduced mobility of the enhancer on loss of SRR107+111 and overall increased mobility on loss of CTCF binding at the SCR (Fig. 4C). When applying GP-FBM to these simulated trajectories, these mobility differences were found to be statistically significant (Fig. 4D), although this manifested as changes in apparent diffusion coefficient, $D_{\alpha\text{-}app}$, rather than anomalous exponent, which was consistently 0.34 for the SCR throughout all the simulations. In line with the expected increased competition between loop extrusion and transcriptional processes being responsible for SCR mobility changes, we found that deletion of SRR107+111 was predicted to increase cohesin occupancy at the adjacent CTCF site (Fig. 4E). Allele-specific chromatin immunoprecipitation (ChIP)–qPCR for Rad21 in *Sox2-SCR*$_{WT}$ and *Sox2-SCR*$_{\Delta SRR107+111}$ cells confirmed this prediction. Cohesin occupancy at the SCR-adjacent CTCF site was significantly increased when the adjacent transcription factor–binding sites, SRR107 and SRR111, are deleted in *cis* ($P = 0.001$; two-tailed *t* test; Fig. 4F). These results suggest that loop extrusion and transcriptional processes not only compete in modulating chromatin architecture as previously reported but also their dynamics. In this case, transcription factor binding or RNA polymerase engagement at the enhancer appears to reduce the amount of cohesin that can extrude through and become stalled at the adjacent CTCF site, thus removing a potent constrainer of chromatin mobility (Fig. 4G). Ours and others' recent observations that transcription forms cohesin-independent TAD borders (*32*, *33*) lead us to favor RNA polymerase as the major contributor.

## DISCUSSION

This work demonstrates that whereas cohesin engagement places a major constraint on chromatin mobility, transcriptional processes also modulate dynamics with potentially important implications for genome regulation. The synchronization of promoter and enhancer dynamics specifically at transcriptional onset is highly evocative in understanding the mechanism of how distal elements may confer gene regulation. A recent body of work favors a model that organizes transcription into specialized nuclear microenvironments or "hubs," whereby high local concentrations of regulatory factors accumulate near genomic sequences that are only loosely coassociated (*34*). Such a model explains findings that enhancers do not need to be directly juxtaposed to gene promoters to influence transcription (*19*, *28*, *35*), and clusters of RNA polymerase and transcription factors have been observed in live nuclei (*36*, *37*). Our results are consistent with, and add further weight, to the hub model. Two seemingly conflicting observations—increased constraint of the SCR and increased diffusion speed of *Sox2*—on transcriptional firing have the net effect of increasing the coupling of promoter-enhancer dynamics, as may be expected when two loci experience the same microenvironment and share the same regulatory factors. Previous results each showed some aspects of our findings (*5*–*9*), but simultaneous tracking of promoter and enhancer motion with transcriptional activity, as well as analytical methods to independently assess the diffusive parameters of each locus was required to unify the view of promoter-enhancer communication in this study. Our findings are not intuitively compatible with sustained enhancer-promoter contacts during transcriptional firing since the gene promoter would also have been expected to experience greater mobility constraints when transcribed. However, without simultaneous measurements of promoter and enhancer mobilities with visualization of hub components, these and other alternative models to transcriptional hubs cannot be excluded. The other important finding of our work was that cohesin-mediated loop extrusion and transcriptional

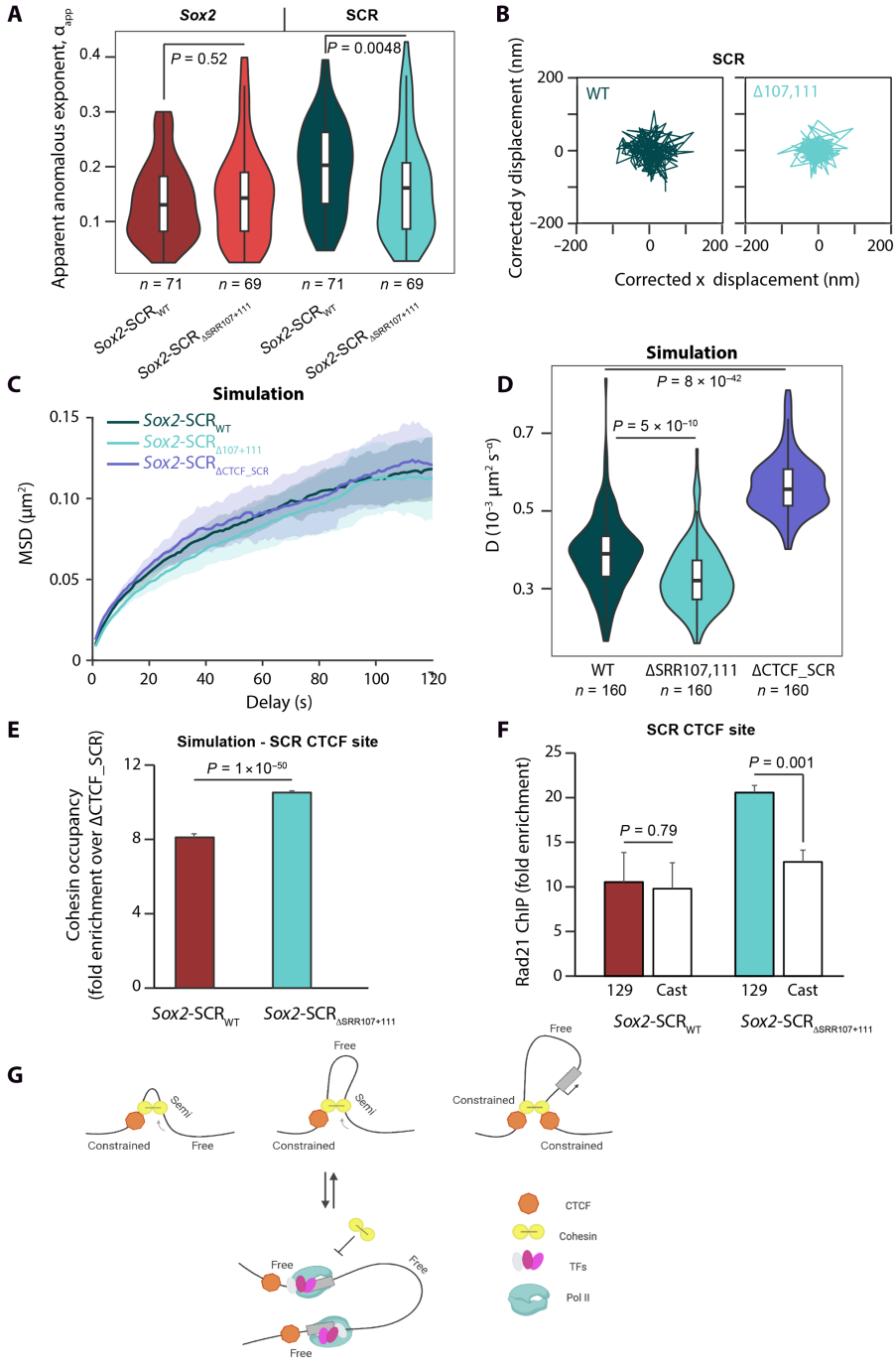


**Fig. 4. Loop extrusion and transcriptional processes compete to constrain chromatin.** (**A**) Violin plot showing distributions of apparent anomalous exponents measured for *Sox2* and SCR in *Sox2-SCR*$_{WT}$ and *Sox2-SCR*$_{\Delta SRR107,111}$ cells. Comparisons are made by Wilcoxon rank sum tests, with *P* values given. (**B**) Sample tracks of 2D trajectories for labeled SCR in *Sox2-SCR*$_{WT}$ and *Sox2-SCR*$_{\Delta SRR107,111}$ cells. Displacements have been corrected for substrate movement, and the plots have been centered on the median positions. (**C**) Ensemble MSD curves for the SCR derived from simulations of wild-type ESCs (dark blue) and those with Δ*SRR107,111* (cyan) or Δ*CTCF-SCR* (purple) when accounting for competition between cohesin and RNA polymerase occupancy. Lines indicate median values and shading the MAD. (**D**) Violin plot showing the distributions of apparent diffusion coefficients derived from simulations for the SCR in *Sox2-SCR*$_{WT}$, *Sox2-SCR*$_{\Delta SRR107,111}$, and *Sox2-SCR*$_{\Delta CTCF\text{-}SCR}$ cells. Comparisons are made by Wilcoxon rank sum tests, with *P* values given. (**E**) Bar chart showing mean expected cohesin occupancy at the SCR-proximal CTCF site, derived from simulations of *Sox2-SCR*$_{WT}$ and *Sox2-SCR*$_{\Delta SRR107,111}$ cells. Comparisons are made by two-tailed *t* test. (**F**) ChIP-qPCR quantification, performed in triplicate, expressed as fold enrichment over a negative control region, of amount of RAD21 binding at the musculus/129 (colored) or castaneus (white) alleles of the SCR CTCF site in *Sox2-SCR*$_{WT}$ and *Sox2-SCR*$_{\Delta SRR107+111}$ cells. Comparisons between allelic binding are made by two-tailed *t* tests, with *P* values given. (**G**) Schematic of competing processes dictating dynamics at the SCR. At the top, extruding cohesin complexes (yellow) place temporary local constraints on mobility of the bound sequences. Such constraints are stabilized when the cohesin encounters bound CTCF (orange) in the appropriate orientation. At the bottom, bound RNA polymerase and transcription factors can also coordinate the *Sox2* and SCR interaction but are refractory to cohesin recruitment and/or extrusion, hence maintaining a relatively more mobile chromatin locus.

processes compete to constrain chromatin dynamics, analogous to their proposed antagonism in organizing chromatin architectures (*29*–*33*). Although SMC complexes are able to bypass RNA polymerase and other large chromatin complexes in vitro (*38*), the implications for transcriptional regulation of the antagonism we and others observe in vivo are very important. Loop extrusion is believed necessary to allow more distal enhancers to search effectively for gene targets (*17*–*19*) but may actually be a barrier itself to forming the transcriptionally competent microenvironment (*32*–*33*). Further elucidation of the potential roles and interactions of transcriptional components and loop extruding complexes in regulation of expression requires experiments beyond current technological capabilities to formally test, simultaneously tagging nuclear proteins, nascent RNA and the promoter and enhancer over sufficiently long time periods to cover multiple transcription cycles while maintaining high temporal resolution. Assessing the potential contribution of cell cycle stage and other cell states to these mechanisms is also an important avenue of future research. Here, using non-perturbing ANCHOR technology with analytical methods for robust and independent measurement of the diffusive parameters of multiple loci, we provide an experimental platform for such ambitious experiments in the future.

## MATERIALS AND METHODS

### Cell lines and culture

Mouse F1 ESCs (*M. musculus*$^{129}$ × *M. castaneus* female cells obtained from B. Panning) were cultured on 0.1% gelatin–coated plates in ESC medium [Dulbecco's modified Eagle's medium (DMEM) containing 15% fetal bovine serum (FBS), 0.1 mM minimum essential medium (MEM) nonessential amino acids, 1 mM sodium pyruvate, 2 mM GlutaMAX, 0.1 mM 2-mercaptoethanol, leukemia inhibitory factor (LIF, 1000 U/ml), 3 μM CHIR99021 (GSK3β inhibitor), and 1 μM PD0325901 (MEK inhibitor)], which maintains ESCs in a pluripotent state in the absence of a feeder layer. The *Sox2-SCR*$_{WT}$ and *Inter-Down* lines were generated by allele-specific CRISPR-Cas9–mediated knock-in of ANCH1 sequence (*23*) into the SCR or downstream control region, and ANCH3 sequence (*5*) into the *Sox2* promoter–proximal region or intervening control region, respectively. Flanking homology arms were first introduced by PCR amplification and Gibson assembly into vectors containing the ANCH1 or ANCH3 sequence, and 1 μg of each vector were cotransfected with 3 μg of plasmid containing Cas9–green fluorescent protein (GFP), a puromycin-resistance marker and a scaffold to encode the two guide RNAs (gRNAs) specific to the two insertion sites [generated by the Institute of Genetics and Molecular and Cellular Biology (IGBMC) molecular biology platform] in 1 million F1 ESCs with Lipofectamine 2000. Single-nucleotide polymorphisms (SNPs) remove the NGG PAM sequence at the *castaneus* allele, assuring allele-specific knock-in (sequences given in table S1). Two days after transfection, the cells were cultured for 24 and then 48 hours with puromycin (with 3 and 1 μg/ml) to enrich for transfected cells before sorting individual GFP-positive cells into 96-well plates and amplification of individual clones. Heterozygous clones with the correct sequences inserted in the *musculus* allele were screened by PCR and sequencing.

The *Sox2-SCR*$_{Rad21}$ and *Inter-Down*$_{Rad21}$ lines were derived from *Sox2-SCR*$_{WT}$ and *Inter-Down* lines, respectively, by CRISPR-Cas9–mediated knock-in of in-frame FKBP$^{F36V}$-HA into both alleles of the 3′ end of *Rad21*. PCR amplification and Gibson assembly was used to replace the homology arms of plasmid pCRIS-PITChv2-dTAG-Puro (BRD4) (Addgene, #91796) with those for *Rad21*, and 1 μg of the vector was cotransfected with 3 μg of plasmid containing Cas9-GFP, a puromycin-resistance marker and a scaffold to encode the gRNA specific to the insertion site (generated by the IGBMC molecular biology platform; sequence of gRNA given in table S1) in 1 million F1 ESCs with Lipofectamine 2000. Two days after transfection, the cells were cultured for 24 and then 48 hours with puromycin (3 and 1 μg/ml) to enrich for transfected cells before sorting individual GFP-positive cells into 96-well plates and amplification of individual clones. Homozygous clones were screened by PCR and sequencing, and dTag13-mediated abrogation of RAD21 was confirmed by Western blot.

*Sox2-SCR*$_{\Delta CTCF\_Prom}$ and *Sox2-SCR*$_{\Delta CTCF\_SCR}$ cells were derived from the *Sox2-SCR*$_{WT}$ line, essentially as in (*27*). One million cells were cotransfected with 2 μg of plasmid containing Cas9-GFP, a puromycin-resistance marker and a scaffold to encode a gRNA targeting the relevant CTCF site (generated by the IGBMC molecular biology platform; sequences given in table S1) and 1 μg of Alt-R homology–directed repair single-stranded DNA oligonucleotide (IDT; sequences given in table S2) with Lipofectamine 2000. The repair oligonucleotides are designed to replace the CTCF motif with an *EcoR*I site to help screening knockouts. Two days after transfection, the cells were cultured for 24 and 48 hours with puromycin (3 and 1 μg/ml) to enrich for transfected cells before sorting individual GFP-positive cells into 96-well plates and amplification of individual clones. Deletions were evaluated on agarose gel after PCR amplification of the region around the deletion and *EcoR*I digestion. Homozygous deletions were confirmed by sequencing.

*Sox2-SCR*$_{\Delta SRR107+111}$ cells were derived from the *Sox2-SCR*$_{WT}$ line, essentially as in (*20*). Briefly, *musculus*-specific deletion of SRR111 was first achieved by cotransfection with plasmids containing four allele-specific gRNAs and Cas9D10A-GFP using Lipofectamine 2000 and then PCR screening as in (*39*). Heterozygous deletion clones were subsequently cotransfected with vectors containing two allele-specific gRNAs and Cas9-GFP to delete SRR107 (sequences given in table S1).

*Sox2-SCR*$_{MS2}$ cells were derived from the *Sox2-SCR*$_{WT}$ line by cotransfecting 1 million cells with 2 μg of plasmid containing Cas9 and the scaffold encoding a gRNA at the *Sox2* 3′UTR, and 2 μg of targeting vector containing the MS2 cassette comprising 24 copies of the v6 MS2 repeat (*40*), a hygromycin resistance cassette flanked by loxP sites, and primer binding sites to facilitate screening for inserted clones, following the strategy in (*41*) (fig. S10), with Lipofectamine 2000. Three days after transfection, cells with integrated vector were selected with 9 days of treatment with hygromycin (200 μg/ml). Individual cells were sorted into 96-well plates for clonal amplification, which were screened for heterozygous (*musculus*-specific) incorporation of full-length 24xMS2 repeats by PCR and sequencing. To remove the selection marker, which may perturb *Sox2* mRNA function, 1 million cells were transfected with 4 μg of Cre-GFP vector with Lipofectamine 2000 and after 3 days were subjected to selection with 6 μM gancyclovir for 10 days. Marker excision and maintenance of full-length MS2 construct were verified by PCR and sequencing in surviving colonies. Last, 1 million cells were cotransfected with 1 μg of ePiggyBac transposase expression plasmid (System Biosciences) and 1 μg each of epB-MCP-mScarletI, epB-OR1–enhanced green fluorescent protein (EGFP), and epB-OR3-IRFP vectors [the OR vectors are derived from those used in (*25*) by adding flanking inverted terminal repeats for recognition by

ePiggyBac transposase; original vectors are available from NeoVirTech] with Lipofectamine 2000. Nine days after transfection, fluorescent cells were sorted in bins (low, medium, and high) on the basis of expression of the different fluorescent proteins and tested by microscopy. Cells with Scarlet$^{high}$/GFP$^{low}$/IRFP$^{low}$ fluorescence were found to be optimal for imaging experiments, and this population was maintained for subsequent experiments.

For differentiation experiments, ESCs were passaged onto laminin-511–coated 35-mm glass-bottom petri dishes, transfected with OR vectors as previously, and switched to DMEM (4.5 g/liter of glucose) supplemented with 2 mM GlutaMAX, 10% FBS, 0.1 mM MEM nonessential amino acids, and 0.1 mM 2-mercaptoethanol without LIF or 2i inhibitors. After 24 hours, the medium was changed daily and supplemented with 5 μM retinoic acid. For RAD21 abrogation experiments, 476 nM dTag-13 (or an equivalent volume of dimethyl sulfoxide as control) was added to the cells and incubated for 2 hours before subsequent experiments.

### Live imaging

Cells were transiently transfected with OR vectors (except for the stably expressing *Sox2-SCR$_{MS2}$* line) and imaged essentially as in (*25*). A total of 150,000 cells were plated 2 days before imaging onto laminin-511–coated 35-mm glass-bottom petri dishes and transfected with 2 μg each of OR1-EFGP and OR3-IRFP plasmids with Lipofectamine 2000. Medium was changed just before imaging to remove dead cells. For fixed controls, the cells were washed with phosphate-buffered saline (PBS), fixed for 20 min with 4% formaldehyde in culture medium at 23°C, and then washed three times for 5 min with PBS before imaging in the same culture medium as used for live cells. Imaging was performed on an inverted Nikon Eclipse Ti microscope equipped with a PFS (perfect focus system), a Yokogawa CSU-X1 confocal spinning disk unit, two sCMOS Photometrics Prime 95B cameras for simultaneous dual acquisition to provide 95% quantum efficiency at 11 μm by 11 μm pixels, and a Leica Objective HC PL APO 100×/1.4 oil. A Tokai Hit Stage incubator allowed for maintenance at 37°C and 5% $CO_2$ throughout the experiment. The system was controlled using Metamorph 7.10 software. For double-label experiments, EGFP and IRFP were excited by 491- and 635-nm lasers. Green and far-red fluorescence were detected with an emission filter using a 525/50-nm and 708/75-nm detection window, respectively. Time lapse was performed in 2D, acquiring 241 time points at 0.5-s interval. Note that we have previously demonstrated that chromatin diffusive properties measured in 2D or 3D yield equivalent conclusions (*42*). For triple-label experiments, EGFP and IRFP were first imaged as for the double label, and then mScarletI was excited at an identical *z* position with a 561-nm laser, and red fluorescence was detected with an emission filter using a 609/54-nm detection window. Time-lapse was performed in 2D, acquiring 301 time points at 1-s interval. For assessment of transcriptional bursting of *Sox2-SCR$_{MS2}$* cells, mScarletI was excited with a 561-nm laser, and red fluorescence was detected with an emission filter using a 609/54-nm detection window. Ten positions were taken per acquisition session, obtaining 20 z-stacks of 0.5-μm interval for each position every 2 min for a total of 2 hours. All time-lapse was performed with PFS of the microscope to avoid any focus drift. A minimum of three biological replicates was performed for each experimental condition, providing a total number of cells between 28 and 100.

### qRT-PCR

Total RNA was extracted using the Nucleospin RNA extraction kit (Macherey-Nagel) and reverse-transcribed using random hexamer primers and SuperScript IV (Invitrogen). qRT-PCR was performed on 10 ng of cDNA aliquots in technical triplicates per biological replicate (three minimum) using QuantitTect SYBR Green PCR kit (Qiagen). Amplification was normalized to *SDHA* (succinate dehydrogenase complex flavoprotein subunit A). SNPs allowed primer design to distinguish *musculus* and *castaneus Sox2* expression (*20*). Primer sequences are given in table S3. Statistical comparisons were made by two-tailed *t* tests.

### Cell cycle analysis

One million cells were fixed in 66% ethanol on ice for 2 hours, washed with PBS, and then resuspended in 750 μl of propidium iodide (50 μg/ml) and ribonuclease A (RNase A, 2 μg/ml) in PBS before incubation at 37°C for 30 min. Analysis of propidium iodide staining with a fluorescence-activated cell sorter Fortesa (BD Biosciences) allowed cells to be gated to $G_1$ (2n DNA content), S (2n < DNA content <4n), and $G_2$-M (4n DNA content) phases. Statistical comparisons from biological replicates were made by two-tailed *t* tests.

### Allele-specific 4C-seq

4C-seq was carried out in biological duplicates, essentially as in (*20*). Cells were fixed with 2% paraformaldehyde in 10% FBS in PBS for 10 min at 23°C. The fixation was quenched with cold glycine at a final concentration of 125 mM, and then the cells were washed with PBS and permeabilized on ice for 1 hour with 10 mM tris-HCl (pH 8), 100 mM NaCl, 0.1% NP-40, and protease inhibitors. Nuclei were resuspended in *Dpn*II restriction buffer at 10 million nuclei/ml concentration, and 5 million nuclei aliquots were further permeabilized by treatment for 1 hour with 0.4% SDS at 37°C and then incubating for a further 1 hour with 3.33% Triton X-100 at 37°C. Nuclei were digested overnight with 1500 U *Dpn*II at 37°C and then washed twice by centrifuging and resuspending in T4 DNA ligase buffer. In situ ligation was performed in 400 μl of T4 DNA ligase buffer with 20,000 U T4 DNA ligase overnight at 23°C. DNA was purified by reverse cross-linking with an overnight incubation at 65°C with proteinase K, followed by RNase A digestion, phenol/chloroform extraction, and isopropanol precipitation. The DNA was digested with *Csp*6I (5 U/μg) at 37°C overnight and then repurified by phenol/chloroform extraction and isopropanol precipitation. The DNA was then circularized by ligation with T4 DNA ligase (200 U/μg) under dilute conditions (3 ng/μl of DNA) and purified by phenol/chloroform extraction and isopropanol precipitation. For *musculus*-specific 4C profiles, samples of the DNA were digested with *Ava*II, cutting specifically at the region between the *Csp*6I site and the non-reading primer annealing site on the *castaneus* allele. A total of 100 ng of aliquots of treated DNA were then used as template for PCR with bait-specific primers containing Illumina adapter termini (primer sequences in table S4). PCR reactions were pooled, primers removed by washing with 1.8× AMPure XP beads, and then quantified on a Bioanalyzer (Agilent) before sequencing with a HiSeq 4000 (Illumina). Sequencing read fastq files were demultiplexed with sabre (https://doi.org/10.5281/zenodo.13853207) and aligned to the mm10 genome with Bowtie (*43*), and intrachromosomal reads were assigned to *Dpn*II fragments by utility tools coming with the 4See package (*44*). 4See was also used to visualize the 4C profiles. Interactions were called for each replicate with

peakC (*45*) with window size set to 21 fragments and were then filtered to only include the regions called as interacting across all wild-type replicates. For statistical comparison of specific interactions, the 4C read counts within 1 Mb of the bait for all replicates and conditions (from the same bait) were quantile normalized using the limma package (*46*). The means of summed normalized 4C scores over tested interacting regions were taken as "interaction scores" and were compared across conditions by two-tailed *t* tests.

### 3D DNA FISH

FISH probes were generated by nick translation from fosmids centered on the ANCHOR insertion sites (WI1-2125O9 for *Sox2*, WI1-788C1 for *Inter*, WI1-111C20 for *SCR*, and WI1-156F5 for *Down*), labeling the DNA with deoxyuridine triphosphate conjugated to biotin (*SCR* and *Down* probes) or digoxigenin (*Sox2* and *Inter* probes). For each hybridization experiment, 300 ng of each probe was combined with 3 μg of mouse $C_0t$ DNA and 20 μg of yeast tRNA and resuspended in 5 μl of hybridization mix [10% (w/v) dextran sulphate, 50% formamide, and 1% Tween-20 in 2× SSC]. Probe was denatured at 95°C for 5 min just before application to cells. FISH was performed as in (*47*). Briefly, the cells were plated on 0.1% gelatin–coated coverslips in ES medium and fixed after 5 hours (before colony formation) for 10 min with 4% paraformaldehyde in PBS, permeabilized for 20 min in 0.5% (w/v) saponin, and incubated for 15 min with 0.1 N HCl, with washes in PBS between each incubation. The cells were then washed in 2× SSC and equilibrated in 50% formamide/2× SSC, before co-denaturing nuclei and probes at 85°C for 5 min and then hybridizing overnight at 37°C in a humidified chamber. The cells were washed three times with 50% formamide/2× SSC at 45°C for 5 min each and then three times with 1× SSC at 60°C for 5 min each before cooling to room temperature in 0.05% Tween-20/4× SSC and blocking for 20 min in 3% bovine serum albumin in 0.05% Tween-20/4× SSC. Anti–digoxigenin-rhodamine and fluorescein-avidin DN were diluted 1:100 in the same blocking solution and incubated with the cells for 1 hour. The cells were washed three times for 5 min in 0.05% Tween-20/4× SSC, and then coverslips were mounted in 4′,6-diamidino-2-phenylindole (DAPI)–containing Vectashield mounting medium. Interphase nuclei were imaged on an LSM 880 AxioObserver (Zeiss) microscope, using a ×63/1.4 objective lens (C plan-Aprochromat 63×/1.4 Oil DIC UV-VIS-IT M27), under 2× zoom and line-averaging four settings. The interval between z slices was 0.37 μm, and the *x*- and *y*-pixel size was 132 nm. Nuclei were segmented, and inter-probe 3D distances were measured by custom scripts in ImageJ (*48*). Distance distribution differences were assessed by Wilcoxon rank sum tests. Measured distances are given in data S1.

### Western blot

For assessing RAD21 abrogation, 3 million cells were collected by trypsinization, washed once in PBS, resuspended in cell lysis buffer [50 mM tris-HCl (pH 7.5), 1 mM EDTA, 150 mM NaCl, 1% Triton X-100, and protease inhibitor cocktail], and incubated on ice for 20 min. Nuclei were collected by centrifugation at 500*g* for 5 min at 4°C, and the pellet was lysed in 50 μl radioimmunoprecipitation assay (RIPA) buffer [50 mM tris-HCl (pH 8), 150 mM NaCl, 1% (v/v) NP-40, 0.5% (w/v) sodium deoxycholate, 0.1% (w/v) SDS, and 1 mM EDTA] for 30 min on ice and then 30 min at 30°C. Lysate was cleared by centrifugation at 22,000*g* for 20 min at 4°C, and protein concentration was measured with a Bio-Rad protein assay. Four micrograms of protein extract was loaded onto an 8% bis-tris polyacrylamide gel for electrophoresis and then transferred to a polyvinylidene difluoride (PVDF) membrane using a Mini Trans Blot Cell (Bio-Rad). Membranes were blocked for 1 hour at 23°C in 4% milk/PBST (0.1% Tween-20 in PBS) and then incubated with primary antibody (anti-Rad21, Abcam ab154769; anti-RNA Pol II CTD4H8, Santa Cruz Biotechnology, #sc-47701) at 1:1000 dilution in 4% milk/PBST overnight at 4°C. Membranes were washed four times for 5 min each at 23°C in PBST and then incubated with 1:10,000 goat anti-mouse alkaline phosphatase (IGBMC) in 4% milk/PBST for 1 hour at 23°C before washing four times for 5 min each at 23°C in PBST and developing with Pierce ECL Western blotting substrate (Thermo Fisher Scientific). Image acquisition was performed on ImageQuant 800 (Amersham).

For assessing SOX2 protein levels in *Sox2-SCR*$_{MS2}$ cells, 3 million cells were collected by trypsinization, washed with PBS, and lysed in 100 μl of RIPA buffer [50 mM tris-HCl (pH 8), 150 mM NaCl, 1% (v/v) NP-40, 0.5% (w/v) sodium deoxycholate, 0.1% (w/v) SDS, and 1 mM EDTA) for 30 min at 4°C. Cell lysate was sonicated with a Covaris E220 Bioruptor in AFA microtubes to shear genomic DNA (peak incident power, 175 W; duty factor, 10%; 200 cycles per burst, 150 s), before addition of 100 U of benzonase (Sigma-Aldrich) in 100 μl of RIPA buffer and incubation for 30 min at 30°C. Lysate was cleared by centrifugation at 22,000*g* for 20 min at 4°C, and protein concentration was measured with a Bio-Rad protein assay. Thirty micrograms of protein extract was loaded onto a 15% bis-tris polyacrylamide gel for electrophoresis and then transferred to a PVDF membrane using a Mini Trans Blot Cell (Bio-Rad). Membranes were blocked for 1 hour at 23°C in 4% milk/PBST and then incubated with primary antibody (anti-Sox2, Santa Cruz Biotechnology, #sc-365823; anti-histone H3, H31HH.3EI- IGBMC) at 1:1000 dilution in 4% milk/PBST overnight at 4°C. Membranes were washed four times for 5 min each at 23°C in PBST and then incubated with 1:10,000 goat anti-mouse-alkaline phosphatase (IGBMC) in 4% milk/PBST for 1 hour at 23°C, before washing four times for 5 min each at 23°C in PBST and developing with Pierce ECL Western blotting substrate (Thermo Fisher Scientific). Image acquisition was performed on ImageQuant 800 (Amersham).

### ChIP-qPCR

For CTCF ChIP, 40 million ESCs were harvested with TrypLE (Invitrogen), fixed for 10 min with 1% formaldehyde, and then quenched with 125 mM glycine for 5 min at 23°C then 15 min at 4°C. The cells were washed with 10% FBS/125 mM glycine in 1× PBS and then lysed in 275 μl of lysis buffer [50 mM tris-HCl (pH 8), 10 mM EDTA, 1% SDS, and 1× complete EDTA-free protease inhibitors] on ice for 20 min. Three hundred and twenty microliters of lysate was transferred to a microtube 500 AFA and sonicated with a Covaris E220 (175 V peak incidence power, 20% duty factor, 200 cycles per burst) for 25 min to shear chromatin to a 200– to 700–base pair range. Cell debris was removed by centrifugation for 15 min at 20,000*g* at 4°C. Equal volumes of protein A- and protein G-Dynabeads (Invitrogen) were mixed and prepared by washing in ChIP dilution buffer [16.7 mM tris-HCl (pH 8), 1.2 mM EDTA, 167 mM NaCl, 1% Triton X-100, 0.01% SDS, and 1× complete EDTA-free protease inhibitors] and then finally resuspending in an equivalent volume of ChIP dilution buffer. One hundred micrograms of chromatin aliquots was diluted eightfold in ChIP dilution buffer and pre-cleared for 90 min with 30 μl of prepared protein A/protein G-Dynabeads at 4°C on a rotating wheel. The precleared chromatin was then incubated overnight at 4°C with 10 μl of either rabbit IgG (1 mg/ml, IGBMC facility) or rabbit anti-CTCF (07-729, Millipore).

Immunoprecipitated chromatin was then adsorbed to 100 μl of prepared protein A/protein G-Dynabeads for 3.5 hours at 4°C on a rotating wheel. The beads were then washed twice for 5 min at 4°C with low-salt wash buffer [20 mM tris-HCl (pH 8), 150 mM NaCl, 2 mM EDTA, 1% Triton X-100, and 0.01% SDS], twice for 5 min at 4°C with high-salt wash buffer [20 mM tris-HCl (pH 8), 500 mM NaCl, 2 mM EDTA, 1% Triton X-100, and 0.01% SDS], twice for 5 min at 4°C with LiCl wash buffer [10 mM tris-HCl (pH 8), 250 mM LiCl, 1 mM EDTA, 1% NP-40, and 1% sodium deoxycholate], and then twice for 5 min at 4°C with TE buffer [10 mM tris-HCl (pH 8) and 1 mM EDTA]. The immunoprecipitated chromatin was eluted by two incubations with 250 μl of elution buffer (100 mM $NaHCO_3$ and 1% SDS) for 15 min at 23°C. Eluate and input samples were decross-linked by treatment overnight at 65°C and then DNA purified by RNase A digestion, proteinase K digestion, phenol/chloroform extraction, and ethanol precipitation. qPCR was performed on one replicate with QuantitTect SYBR Green PCR kit (Qiagen) using dilutions of the input material to generate the standard curve. Primer sequences are given in table S5.

For RAD21 ChIP, performed in biological triplicate, 40 million ESCs were fixed for 45 min with 2 mM succinimidyl glurarate and then for 10 min with 1% formaldehyde at 23°C before quenching with 125 mM glycine for 15 min at 23°C. Cell pellets were washed twice with ice-cold PBS and then resuspension and incubation in lysis buffer 1 [50 mM Hepes-KOH (pH 7.5), 140 mM NaCl, 1 mM EDTA, 10% glycerol, 0.5% NP-40, and 0.25% Triton X-100] for 10 min at 4°C. Lysates were centrifuged for 5 min at 2000*g* at 4°C before incubation for 10 min at 4°C in lysis buffer 2 [10 mM tris-HCl (pH 8), 200 mM NaCl, 1 mM EDTA, and 0.5 mM EGTA]. Lysates were again centrifuged for 5 min at 2000*g* at 4°C before resuspension in ice-cold lysis buffer 3 [10 mM tris-HCl (pH 8), 100 mM NaCl, 1 mM EDTA, 0.5 mM EGTA, 0.1% sodium deoxycholate, and 0.5% *N*-laurylsarcosine]. Chromatin was sonicated in a probe sonicator at 20 A (15-s on/30-s off) for 2.5 min at 4°C. Triton X-100 was added to the sonicated lysate to precipitate any remaining debris, and the cleared lysate was incubated overnight with 5 μg of anti-Rad21 antibody (Abcam, ab217678) at 4°C with rotation. Protein A/G Dynabeads (80 μl, Invitrogen) was added to the antibody-bound chromatin and incubated overnight at 4°C with rotation. The immunoprecipitates were washed six times at 23°C with RIPA buffer followed by a tris-buffered saline buffer wash, and then the bound chromatin was eluted by incubation for 30 min at 65°C with elution buffer [50 mM tris-HCl (pH 8), 10 mM EDTA, and 1% SDS] before the addition of 4 μl of proteinase K (20 mg/ml) and reversal of cross-links by incubation at 65°C overnight. DNA was purified with phenol/chloroform extraction and ethanol precipitation before qPCR quantification (primer sequences given in table S5) using serial dilutions of pre-immunoprecipitated input material to generate the quantification standard curve. Quantification at the musculus and castaneus SRR109 (SCR CTCF site) was expressed as fold enrichment over the amplification at a non-genic, negative control sequence, not bound by RAD21, CTCF, or known pluripotency transcription factors.

### Single-molecule RNA FISH

MS2v6 and *Sox2* probes were designed with Stellaris Probe Designer and labeled with Cy3 and Cy5, respectively, on the 3′ ends. Glass coverslips were placed into a 12-well plate and coated overnight with poly-D-lysine. A total of 400,000 cells were seeded per well and allowed to attach for 3 hours to 70 to 80% confluency at 37°C at 5% $CO_2$. The cells were washed three times with prewarmed Hanks' balanced salt solution buffer (no calcium, magnesium, or phenol red; Thermo Fisher Scientific) before aspiration of buffer, cell fixation in 4% paraformaldehyde in PBS for 10 min at 23°C, and then two washes in PBS for 10 min at 23°C. The cells were permeabilized overnight in 70% ethanol at 4°C and then washed for 5 min at 37°C with prewarmed wash buffer [10% (v/v) formamide in 2× SSC]. Coverslips were aspirated and dried for 5 min before application of hybridization mix [50 nM each probe in 10% (w/v) dextran sulphate sodium salt, 10% (v/v) formamide, and 2× SSC] and incubation overnight at 37°C in a humidified chamber. Coverslips were washed three times in wash buffer for 30 min at 37°C and then rinsed in 2× SSC and washed in PBS for 5 min at 23°C. The samples were mounted in Prolong Gold with DAPI (Invitrogen) on glass slides and left to dry in the dark for 24 hours before imaging on a Zeiss AxioObserver 7 inverted wide-field fluorescence microscope with light-emitting diode (LED) illumination (SpectrX, Lumencor) and sCMOS ORCA Flash 4.0 V3 717 (Hamamatsu). A 40× oil objective lens (numerical aperture, 1.4) with 1.6× Optovar was used. Twenty-seven z-stacks with 300-nm slices and 1 × 1 binning were taken with an exposure time of 500 ms for Cy3, 750 ms for Cy5 (100% LED power for both), and 25 ms for DAPI (10% LED power). Micromanager 1.4 software was used. A custom Python script was used to detect, localize, and classify the spots (https://doi.org/10.5281/zenodo.13833958). Cells and nuclei were segmented using Otsu thresholding and watershedding. Spots were localized by fitting a 3D Gaussian mask after local background subtraction (*49*) and counted per cell. To estimate transcriptional bursting frequencies, the same scripts identified the two brightest spots with the nucleus (assuming two alleles per cell) and normalized their intensity to the average intensity of cytoplasmic signals (assumed to be single mRNA molecules). Nuclear foci with >2.5-fold stronger intensity than the cytoplasmic average were inferred to be bursting sites and were counted. A minimum of 1500 cells were analyzed for each condition.

### Localizing and tracking chromatin loci

Live imaging experiments were treated essentially as in (*25*). First, spot detection and tracking were performed with ICY (*50*) before localization precision enhancement in GPTool (*25*). This assumes that the spots have the shape of a 2D Gaussian function, as follows,

$$S_{x,y} = I_o \, exp\left\{-\frac{1}{2}\begin{pmatrix} x-\mu_x \\ y-\mu_y \end{pmatrix}^T \begin{bmatrix} L_x^2 & \theta L_x L_y \\ \theta L_x L_y & L_y^2 \end{bmatrix}^{-1} \begin{pmatrix} x-\mu_x \\ y-\mu_y \end{pmatrix}\right\} + B_G$$

with $\mu_i$ representing the center of mass of the spot, $L_i$ its size in directions $x$ and $y$, $-1 < \theta < 1$ a possible rotation, while $B_G$ and $I_o$ are background and spot signal, respectively. The localization is optimized using the NM-Simplex method, and localization error is estimated using the Metropolis-Hastings algorithm. Any outlier detection events, defined as having any of the signal intensity, spot size, or localization error deviating from the median value within the experiment by more than twice the interquartile range, were removed from subsequent analysis. For the *Sox2-SCR$_{MS2}$* line, ICY was additionally used for spot detection and tracking of MCP (mScarletI). Most experiments had MCP detection for virtually all or none of the frames and were categorized as "transcribing" and "non-transcribing" cells, respectively. The other experiments were only included in the analysis if they contained at least 75 contiguous frames with MCP signal (transcribing) and/or absence (non-transcribing). For these, the largest contiguous stretch of frames above this threshold was maintained for subsequent analysis.

### Inter-probe distance measurements and determination of precision

For inter-spot distance measurements, effects of camera misalignments and chromatic aberrations were corrected as in (*25*) with a set of generic affine transformations, including translation, rotation, and scaling, defined as,

$$\Omega = \begin{pmatrix} s_x & 0 & (1-s_x)W/2 \\ 0 & s_y & (1-s_y)H/2 \\ 0 & 0 & 1 \end{pmatrix} \begin{pmatrix} 1 & 0 & d_x+c_x \\ 0 & 1 & d_y+c_y \\ 0 & 0 & 1 \end{pmatrix} \begin{pmatrix} \cos(\theta) & \sin(\theta) & 0 \\ -\sin(\theta) & \cos(\theta) & 0 \\ 0 & 0 & 1 \end{pmatrix} \begin{pmatrix} 1 & 0 & -c_x \\ 0 & 1 & -c_y \\ 0 & 0 & 1 \end{pmatrix}$$

where $s_i$ accounts for scaling in directions $x$ and $y$, $d_i$ accounts for translation in both directions, and θ is the angle of rotation between both channels in relation to point $c_i$. To infer optimal parameters for correction, five frames from each of the movies recorded in the session were used and the likelihood was maximized using the Nelder-Mead simplex method,

$$\log P \propto -\frac{WH}{2} \log\left\{\sum_{k,l}\left[I_2(k,l\,|\,\Omega) - I_1(k,l\,|\,\mathbb{1})\right]^2\right\}$$

where $W$ and $H$ correspond to width and height of images, and $I_r(k,l|A)$ is the value of pixel $(k,l)$ in channel r given transformation A. Here, $\mathbb{1}$ represents the identity matrix. After applying these transformations to the final localized spots, the 2D distances between two spots are then computed in a Pythagorean framework. The median distances were taken for each imaging experiment.

To determine the precision of these measurements in our live imaging setup (fig. S2), a tracer plasmid was constructed by PCR amplification and Gibson assembly, containing ANCH1 (*parS*) and the ParB sequences, OR1-IRFP and OR1-EGFP, and transiently transfected into F1 ESCs. Live imaging was performed as before, except that only 20 frames (two frames per second) were taken, with the focal plane containing several ANCH1 spots labeled with both OR1 fluorophores, which in theory have zero physical separation. The above corrections were performed on the images, and the shortest IRFP-to-EGFP distances were recorded, representing the precision error of the measurements.

### GP-FBM measurement of diffusive parameters

Diffusive parameters for individual trajectories were estimated using GPTool (*25*), which assumes that the stochastic diffusion trajectory of a chromatin locus can be modeled as a Gaussian process with the following fractional Brownian kernel

$$\Sigma_{D_\alpha,\alpha}(t,t') = D_\alpha\left(|t|^\alpha + |t'|^\alpha - |t-t'|^\alpha\right)$$

producing generalized Brownian motion with MSD

$$\langle r^2\rangle = 2nD_a t^\alpha$$

where $n$ corresponds to the number of degrees of freedom. Formal derivation of the model and details of the methods used to optimize the model fit are found in (*25*) and references within. Experimental trajectories were verified as being reasonably fit by a fractional Brownian regime by checking that displacements are self-similar Gaussian distributed with the modeled covariance matrix (fig. S3) and that the velocity autocorrelation function from experimental trajectories,

$$C_v^{(\varepsilon)}(\tau) = \frac{1}{\varepsilon^2}\langle[x(\tau+\varepsilon)-x(\tau)][x(\varepsilon)-x(0)]\rangle$$

with velocity defined as $v(\tau) = \varepsilon^{-1}[x(\tau+\varepsilon) - x(\tau)]$, fits the theoretical velocity autocorrelation function for FBM (fig. S4)

$$\frac{C_v^{(\varepsilon)}(\tau)}{C_v^{(\varepsilon)}(0)} = \frac{(\tau+\varepsilon)^\alpha - 2\tau^\alpha + |\tau-\varepsilon|^\alpha}{2\varepsilon^\alpha}$$

To measure and correct for substrate movement, GPTool builds a covariance model to handle the cross-correlation that substrate motion introduces into the two measured particles' trajectories, generating the probability distribution

$$\rho(r_1, r_2\,|\,\alpha, D_\alpha) \propto exp\left\{-\frac{1}{2}\begin{pmatrix} r_1 \\ r_2 \end{pmatrix}^T \begin{pmatrix} \Sigma_1+\Sigma_R & \Sigma_R \\ \Sigma_R & \Sigma_2+\Sigma_R \end{pmatrix}^{-1} \begin{pmatrix} r_1 \\ r_2 \end{pmatrix}\right\}$$

where $\Sigma_1$, $\Sigma_2$, and $\Sigma_R$ are FBM covariance matrices for the two particles and substrate, respectively, with diffusion parameters $D_\alpha = \{D_{\alpha1}, D_{\alpha2}, D_{\alpha R}\}$ and $\alpha = \{\alpha_1, \alpha_2, \alpha_R\}$. Formal derivation of the model and details of the methods used to optimize the model fit are found in (*25*) and references within. Overall, GPTool outputs, for each individual imaging experiment: more precise trajectories for the two particles; estimations of diffusive parameters $D_\alpha$ and α for each particle, with and without substrate correction; estimations of the trajectory of the substrate, as well as its diffusive parameters, $D_{\alpha R}$ and $\alpha_R$. The distributions of inferred parameters from different genomic loci or experimental conditions were visualized by violin plots generated with the ggplot2 package of R and compared by Wilcoxon rank sum test, with Benjamini-Hochberg multiple-testing correction in cases where four or more statistical tests were combined. All trajectories and inferred diffusive parameters are reported in data S3.

For the analysis presented in fig. S7E, we applied GP-FBM directly to the 3D trajectories inferred for the transgenic constructs described in (*15*), with the original authors' methods for tracking and measuring the labeled loci to provide a fully orthologous comparison. This study contains site-specific insertions of TetO and lacO tags at a genomic separation of ~150 kb, with or without three copies of convergently oriented CTCF sites. We also applied analysis to trajectories from lines containing the CTCF sites on only the lacO or TetO side of the construct, allowing us to compare dynamics with locally and/or distally bound CTCF sites (data S2). We note that the inferred apparent anomalous exponents (~0.2) are similar to what was measured for loci in this study, although the transgenic construct movies were made in 3D and for longer periods of time (~3 hours) at lower temporal resolution (2 frames/min).

### Trajectory plots

To generate the individual trajectory plots (e.g., Fig. 1E), the inferred substrate motion at each time interval was subtracted from the $x$ and $y$ coordinates of the GPTool-refined tracked particles and then multiplied by the scaling factor (110 nm per pixel) to obtain corrected coordinates in nanometers for the particle at each time point. The deviation of these values from the median $x$ or $y$ value, respectively, of the trajectory were plotted, maintaining their temporal order, to generate comparable trajectory plots across experiments centered on the origin.

### MSD analysis

MSD analysis was performed using the msdanalyzer utility in Matlab (*51*). For each individual trajectory, the time-averaged MSD was computed (time steps of 0.5 to 120 s for most experiments; 1 to 300 s for experiments with the *Sox2-SCR*$_{MS2}$ line), using either the trajectories uncorrected or corrected by GPTool for substrate movement, as

stated. Because some trajectories exhibited large deviations from the average, especially at long time, we chose to calculate the ensemble median of all individual MSD and the MAD as a measure of the variability. For testing the fit of GPTool-measured parameters to experimental data, theoretical 2D MSD curves were made from these measured parameters for each individual trajectory, giving either

$$MSD = 4D_{\alpha,uncorr}t^{\alpha,uncorr}$$

for parameters called without substrate correction, or

$$MSD = 4D_{\alpha,corr}t^{\alpha,corr} + 4D_{\alpha,substrate}t^{\alpha,substrate}$$

for the particle and substrate parameters called when substrate motion correction is applied. The ensemble medians of these MSD curves were plotted with the experimental MSD curves. Radial MSD was computed in exactly the same way as single-particle MSD but using the evolution of Euclidean distance between two particles instead of the displacement of a single particle. The diffusive parameters were fit to the first 60 s of the log-log plots of radial MSD using linear least squares with bisquare weights, implemented in Matlab. 95% confidence intervals were estimated as two SDs of the point estimates. Diffusive parameter differences between *Sox2*-SCR and *Inter-Down* radial MSD were assessed by ANCOVA.

### Assessing localization errors

The localization error has been measured for both eGFP and iRFP channels on fixed cells by measuring their MSD over time, in the same way as for living cells. This error is due to the fluctuations of emitting photons from the fluorescent probes and recorded by the photodiode after correction of noisy motion from the microscope stage by our GP-FBM framework. One needs to pay attention to the fact that the displacements for fixed cells are inferior to the pixel size (110 nm), which is a major asset of our GP-FBM framework since the noisy motions of the microscope stage are usually the critical corrections for single-particle tracking. As can be seen in fig. S5B, the distributions of alpha exponents for fixed cells are close to zero, which indicates that the localization error mainly arises from instrumental origins (the ones listed above).

### Transcriptional bursting measurements

Using the LiveCell pipeline (https://doi.org/10.5281/zenodo.13833958) (*52*), maximal intensity projections were made of the 3D movies, followed by background subtraction and cell segmentation using Otsu thresholding and watershedding. Transcription bursts were detected and tracked using a 2D Gaussian fit followed by hysteresis filtering using 5 and 8 SDs of the background as low/high thresholds, respectively. Output data were manually checked to reject erroneous tracking or dividing cells.

### Molecular dynamics simulations

Molecular dynamics simulations were performed via the multipurpose EspressoMD package (*53*) as in (*29*). Individual proteins are represented by "beads" interacting via phenomenological force fields and move according to the Langevin equation, and the chromatin fiber is represented as a chain of beads connected by bonds. The position of every bead in the system evolves according to the Langevin differential equation that encodes Newton's laws in the case of thermal bath with the friction γ due to an implied solvent in the presence of forces between beads encoded by energy potential functions *U* (*54*, *55*). Langevin equations for all beads are simultaneously solved in EspressoMD using a standard Velocity-Verlet numerical algorithm. The potential connecting *i* and *i + 1* beads of the fiber is a finitely extensible nonlinear elastic (FENE) spring that adds up to a steric repulsion potential between nonadjacent sites of the polymer, the Weeks-Chandler-Andersen potential

$$U_{FENE} = -\frac{K_{FENE}R_0^2}{2} ln\left[1 - \left(\frac{r_{i,i+1} - r_0}{R_0}\right)\right]$$

$$U_{WCA} = \begin{cases} 4\epsilon\left[\left(\frac{\sigma}{r}\right)^{12} - \left(\frac{\sigma}{r}\right)^{6} + \frac{1}{4}\right] \text{ if } r < \sigma 2^{1/6} \\ 0 \text{ otherwise} \end{cases}$$

where $r_{i,i+1}$ is the distance between consecutive beads, and σ is where the interaction from repulsive becomes attractive and can be interpreted as the diameter of the particles. This value is a natural length scale of the system. In FENE, the parameters are fixed to have an equilibrium distance of 1.6 σ with maximum extension of 0.8 σ and a bond energy of $K_{FENE} = 30$ $k_BT$. Since the fiber is resolved at 1 kb, chromatin rigidity cannot be neglected (i.e., below the persistence length). Bending rigidity of the polymer is introduced via the Kratky-Porod potential for every three adjacent chromatin beads, where θ is the angle between three consecutive beads as given by

$$U_{KP}(\theta) = K_{BEND}[1 - \cos(\theta)]$$

and $K_{BEND}$ is the bending energy. The persistence length in units of σ is given by $L_p = K_{BEND}/k_BT$. The model includes (i) full 3D loop extrusion by interplay of cohesin dimers and CTCF and (ii) transcription by Pol II particles. To simulate association of cohesin and Pol II with chromatin, a harmonic potential was used, mimicking formation of a stable bond between two particles that fluctuate around an equilibrium distance $d_0$

$$U_H = \frac{1}{2}K_H\left(r - d_0\right)^2$$

From now on, any description of the formation of a bond means the introduction of the aforementioned harmonic bond between the particles involved. To regulate the lifetime of these harmonic interactions, mechanisms of bond formation and removal were introduced according to cutoff distance $c_d$ below which a bond is formed, with a certain probability rate of detachment in units of time $\tau_b = 2\tau$ (τ being the fundamental unit of time in molecular dynamics; see below). These are then set to approximate the experimentally observed range of Pol II transcription and cohesin loop extrusion speeds and chromatin residence time. Introduction of the above mechanics is added on top of the strings-binders-switch model (*56*), which encodes the association tendency of Pol II with the *Sox2* promoter (defined as the 1-kb bead containing the transcription start site within the modeled region) by means of the shifted, truncated Lennard-Jones (LJ) potential, allowing spontaneous colocalization of beads around a distance σ with lifetime and stability properties depending on the depth of the energy well ϵ

$$U_{LJ} = \begin{cases} 4\epsilon\left[\left(\frac{\sigma}{r}\right)^{12} - \left(\frac{\sigma}{r}\right)^{6} + c_{shift}\right] \text{ if } r < r_{\text{cut}} \\ 0 \text{ otherwise} \end{cases}$$

where $r_{cut}$ is a cutoff distance, $r$ is the separation of any two beads, and $r_{cut} = 2.5\sigma$ for all LJ potentials in the simulations. This is a standard commonly used in the field to simulate phenomenological coarse-grained affinities (*54*, *55*).

For Pol II interactions and transcription, the polymerase is presented as a bead with LJ interaction with specific beads of the chromatin fiber representing the promoter, enhancers (defined as beads containing H3K27ac peaks), or gene body (beads containing *Sox2* coding sequence) with energy $\epsilon = 2\ k_BT$. Such mild affinity helps to identify promoters as the correct sites where transcription initiation will take place (i.e., Pol II forming stable bonds with the promoter bead) before the elongation process starts along the gene body. LJ interactions were also introduced among Pol II beads ($\epsilon = 2.5\ k_BT$), to simulate their tendency to form condensates acting as transcription hubs, and between Pol II and cohesin ($\epsilon = 2\ k_BT$) to simulate preferential loading of cohesin at promoter/enhancer beads. Pol II transcription dynamics are simulated as a four-step process: attachment to the promoter in an exclusive manner, elongation starts, elongation proceeds through the gene body, and detachment at the transcription termination site (the end of the gene body). A bond forms if the beads are less distant in space than a certain cutoff (2.7 σ). To simulate the tendency of Pol II to reel in gene body beads, a secondary bond is formed with the next bead on the chromatin fiber in the direction of transcription ($i + 1$ bead, where $i$ is the promoter coordinate on the fiber, and if transcription occurs in the sense direction; $i$-1 in the antisense direction). In the next step, Pol II moves on the next site by forming new bonds with $i + 1$ site and dissolving the old ones with $i$. This happens at a given rate ($0.4\ \tau_b^{-1}$) and only if the beads are found closer than a cutoff distance ($c_d = 1.05\ \sigma$). These values are selected to obtain a Pol II transcription speed approximately in the range of 1 to 10 kbp/min observed experimentally. Upon reaching the transcription end site (TES), Pol II stops and becomes unbound with rate 0.2 τb. Upon binding with promoters, Pol II loses its LJ interaction with promoters since this is substituted by the bond itself. Pol II is also allowed to form bonds with enhancers, although, in this case, no transcription procedure is initiated. Because the model does not allow cohesin and Pol II to bind to the same chromatin bead simultaneously, their effective competition can be modulated by altering the rate of Pol II bond dissolution at enhancers. The initial model was set at two bonds lost per second and did not recapitulate phenotypic effects on SRR107+111 deletion (fig. S9D). Reinforced transcription-loop extrusion competition, recapitulating phenotypic effects (Fig. 4), sets bond dissolution to 0.5 bonds per second. Cohesin concentration was maintained at 20 nM in the models.

For CTCF binding, a single bead interacts via LJ potential ($\epsilon = 2\ k_BT$) with specific beads of the chromatin fiber [CTCF ChIP sequencing (ChIP-seq) peaks containing oriented cognate binding motifs]. Once a bond is formed (with rate $0.8\ \tau b^{-1}$), it is pair exclusive (i.e., other CTCF molecules cannot bind that same site). The bond dissolves at the rate $2 \times 10^{-5}\ \tau b^{-1}$ and CTCF is again free to diffuse and search for other binding sites. Cohesin is represented as a pair of beads connected by one bond ($r_0 = 1.6\ \sigma$ and $K = 8\ k_BT$). Extrusion has three steps: attachment, active extrusion, and detachment. For attachment, each cohesin monomer forms a bond with the chromatin fiber. Bonds form when a cohesin monomer and a chromatin site come within a given cutoff distance (1.6 σ) and at a certain rate ($0.1\ \tau_b^{-1}$). Only the case where both monomers simultaneously form bonds on adjacent chromatin beads is considered a successful attachment and the dimer is retained for the next step; otherwise, bonds dissolve. If a promoter is already engaged in a bond with Pol II, cohesin is forbidden to bind that promoter. In addition, to favor cohesin loading in correspondence of active transcribing promoters, a 90% chance of binding has been introduced when a cohesin molecule is close to a promoter/enhancer, and, at the same time, one Pol II is close by as well (cutoff distance, 1.5 σ); otherwise, cohesin binding chance drops to 10%. The active extrusion and detachment steps follow the same mechanics as for Pol II, with the difference that Pol II can reel through cohesin bound sites while the inverse is not allowed. New bonds are formed if the distance is below 1.1 σ. Such parameters produce ranges of cohesin extruding speed of 15 to 30 kb/min, which is within the range of experimentally observed values (*30*). This allows cohesin to be affected by the surroundings during extrusion (e.g., presence of Pol II close by or bound to adjacent sites). Cohesin detachment can occur independently at any step at a given rate ($10^{-4}\ \tau_b^{-1}$) to fit its known chromatin residence time of 20 min. CTCF "loop anchors" are modeled so that cohesin cannot form new bonds with the next $i \pm 1$ site if the latter is already bound by CTCF, provided that it has the binding motif in convergent orientation. This renders extrusion dependent on CTCF dynamics. Last, cohesin has LJ affinity for Pol II both in the bound ($\epsilon = 2.5\ k_BT$) and unbound state ($\epsilon = 2\ k_BT$, higher affinity for bound Pol II mimicking its suggested role in cohesin loading on chromatin). Pol II and loop extrusion dynamics are performed using a python script driving the EspressoMD library. The polymer initializes as a random walk and its dynamics first evolves in the absence of extrusion and transcription to generate an equilibrium coil formation. Extrusion and transcription processes are then switched on, and the evolution of the bead positions is tracked. Across all simulations, standard values for the friction coefficient ($\gamma = 0.5$) and the time step ($t = 0.01$) are used. To connect in silico space-time units with real distances and times, it is assumed that the concentration of DNA in the 3D simulation space is the same as that in a mammalian nucleus, giving a rough estimation of $\sigma = 52$ nm. For time units, the standard molecular dynamics relation $\tau = \eta(6\pi\sigma^3/\epsilon)$ is used. Assuming a viscosity ~0.5 P, the fundamental time unit is $\tau = 0.017$ s. Concentrations of CTCF and Pol II are taken from the physiological values and range from 30 to 60 nM. The energy scale of the system is given by the Boltzmann factor $k_B$ multiplied by the temperature of the system T = 310 K.

The region modeled (mm10; chr3:34.3-35.1 Mb) encompasses the *Sox2* gene, 16 enhancer beads from the peaks of H3K27ac, and six CTCF-binding regions with directionality determined by orientation of binding motifs. CTCF-binding regions can be composed of up to three beads where CTCF occupancy signal is the highest (i.e., two regions upstream of *Sox2*), giving a stronger anchoring function to such regions. Polymer models for *Sox2-SCR*$_{\Delta CTCF\_Sox2}$ and *Sox2-SCR*$_{\Delta CTCF\_SCR}$ have the relevant CTCF sites converted into non–CTCF-binding beads to remove the cohesin anchoring effect. The model for *Sox2-SCR*$_{\Delta SRR107,111}$ has the two enhancer beads immediately flanking the SCR CTCF region completely removed from the polymer and reduced Pol II stability to the promoter (from 0.02 to 0.2 bonds lost per second) to mimic inactivation of the gene. The positions of the beads corresponding to the positions of ANCHOR labels were tracked across 40 simulations of 1000 time points, and these trajectories were subsequently fed into MSD fits and GPTool diffusive parameter estimations, as for the experimental trajectories.

## Data sources

ESC and NPC Hi-C data were taken from (*26*) and reanalyzed and visualized using FAN-C (*57*). The differential Hi-C map was derived

as in (*33*). The normalized scores of the ESC Hi-C submatrix were subtracted from those of the NPC Hi-C submatrix, and the difference was expressed as a *z* score: [diff – mean(diff)]/SD(diff). Insulation was computed using FAN-C with a binsize of seven bins (28 kb). ESC ChIP-seq datasets for H3K27ac, CTCF, and RAD21 were obtained from the CODEX database (*58*). For comparison of 2D *Sox2*-SCR distance distributions with analogous methods, results from oligoFISH were taken from (*24*).

## Supplementary Materials

**The PDF file includes:**
Figs. S1 to S10
Tables S1 to S5
Legends for movies S1 to S4
Legends for data S1 to S3

**Other Supplementary Material for this manuscript includes the following:**
Movies S1 to S4
Data S1 to S3

## REFERENCES AND NOTES


1. T. Sexton, G. Cavalli, The role of chromosome domains in shaping the functional genome. *Cell* **160**, 1049–1059 (2015).
2. S. Schoenfelder, P. Fraser, Long-range enhancer-promoter contacts in gene expression control. *Nat. Rev. Genet.* **20**, 437–455 (2019).
3. T. Lionnet, C. Wu, Single-molecule tracking of transcription protein dynamics in living cells: Seeing is believing, but what are we seeing? *Curr. Opin. Genet. Dev.* **67**, 94–102 (2021).
4. M. M. Tortora, H. Salari, D. Jost, Chromosome dynamics during interphase: A biophysical perspective. *Curr. Opin. Genet. Dev.* **61**, 37–43 (2020).
5. T. Germier, S. Kocanova, N. Walther, A. Bancaud, H. A. Shaban, H. Sellou, A. Z. Politi, J. Ellenberg, F. Gallardo, K. Bystricky, Real-time imaging of a single gene reveals transcription-initiated local confinement. *Biophys. J.* **113**, 1383–1394 (2017).
6. H. Ochiai, T. Sugawara, T. Yamamoto, Simultaneous live imaging of the transcription and nuclear position of specific genes. *Nucleic Acids Res.* **43**, e127 (2015).
7. T. Nozaki, R. Imai, M. Tanbo, R. Nagashima, S. Tamura, T. Tani, Y. Joti, M. Tomita, R. Hibino, M. T. Kanemaki, K. S. Wendt, Y. Okada, T. Nagai, K. Maeshima, Dynamic organization of chromatin domains revealed by super-resolution live-cell imaging. *Mol. Cell* **67**, 282–293.e7 (2017).
8. R. Nagashima, K. Hibino, S. S. Ashwin, M. Babokhov, S. Fujishiro, R. Imai, T. Nozaki, S. Tamura, T. Tani, H. Kimura, M. Shribak, M. T. Kanemaki, M. Sasai, K. Maeshimi, Single nucleosome imaging reveals loose genome chromatin networks via active RNA polymerase II. *J. Cell Biol.* **218**, 1511–1530 (2019).
9. B. Gu, T. Swigut, A. Spencley, M. R. Bauer, M. Chung, T. Meyer, J. Wysocka, Transcription-coupled changes in nuclear mobility of mammalian cis-regulatory elements. *Science* **359**, 1050–1055 (2018).
10. J. R. Dixon, S. Selveraj, F. Yue, A. Kim, Y. Li, Y. Shen, M. Hu, J. S. Liu, B. Ren, Topological domains in mammalian genomes identified by analysis of chromatin interactions. *Nature* **485**, 376–380 (2012).
11. T. Sexton, E. Yaffe, E. Kenigsberg, F. Bantignies, B. Leblanc, M. Hoichman, H. Parrinello, A. Tanay, G. Cavalli, Three-dimensional folding and functional organization principles of the *Drosophila* genome. *Cell* **148**, 458–472 (2012).
12. I. F. Davidson, J. M. Peters, Genome folding through loop extrusion by SMC complexes. *Nat. Rev. Mol. Cell Biol.* **22**, 445–464 (2021).
13. Y. Li, J. H. I. Haarhuis, A. S. Cacciatore, R. Oldenkamp, M. S. van Ruiten, L. Willems, H. Teunissen, K. W. Muir, E. de Wit, B. D. Rowland, D. Panne, The structural basis for cohesin-CTCF-anchored loops. *Nature* **578**, 472–476 (2020).
14. M. Gabriele, H. B. Brandão, S. Grosse-Holz, A. Jha, G. M. Dailey, C. Cattoglio, T.-H. S. Hsieh, L. Mirny, C. Zechner, A. S. Hansen, Dynamics of CTCF- and cohesin-mediated chromatin looping revealed by live-cell imaging. *Science* **376**, 496–501 (2022).
15. P. Mach, P. I. Kos, Y. Zhan, J. Cramard, S. Gaudin, J. Tünnermann, E. Marchi, J. Eglinger, J. Zuin, M. Kryzhanovska, S. Smallwood, L. Gelman, G. Roth, E. Nora, G. Tiana, L. Giorgetti, Cohesin and CTCF control the dynamics of chromosome folding. *Nat. Genet.* **54**, 1907–1918 (2022).
16. N. Kubo, H. Ishii, X. Xiong, S. Bianco, F. Meitinger, R. Hu, J. D. Hocker, M. Conte, D. Gorkin, M. Yu, B. Li, J. R. Dixon, M. Hu, M. Nicodemi, H. Zhao, B. Ren, Promoter-proximal CTCF binding promotes distal enhancer-dependent gene activation. *Nat. Struct. Mol. Biol.* **28**, 152–161 (2021).
17. L. Kane, I. Williamson, I. M. Flyamer, Y. Kumar, R. E. Hill, L. A. Lettice, W. A. Bickmore, Cohesin is required for long-range enhancer action at the *Shh* locus. *Nat. Struct. Mol. Biol.* **29**, 891–897 (2022).
18. N. J. Rinzema, K. Sofiadis, S. J. D. Tjalsma, M. J. A. M. Verstegen, Y. Oz, C. Valdes-Quezada, A. K. Felder, T. Filipovska, S. van der Elst, Z. de Andrade Dos Ramos, R. Han, P. H. L. Krijger, W. de Laat, Building regulatory landscapes reveals that an enhancer can recruit cohesin to create contact domains, engage CTCF sites and activate distant genes. *Nat. Struct. Mol. Biol.* **29**, 563–574 (2022).
19. M. Du, S. H. Stitzinger, J.-H. Spille, W. K. Cho, C. Lee, M. Hijaz, A. Quintana, I. I. Cissé, Direct observation of a condensate effect on super-enhancer controlled gene bursting. *Cell* **187**, 331–344.e17 (2024).
20. T. Taylor, N. Sikorska, V. M. Shchuka, S. Chahar, C. Ji, N. N. Macpherson, S. D. Moorthy, M. A. C. de Kort, S. Mullany, N. Khader, Z. E. Gillespie, L. Langroudi, I. C. Tobias, T. L. Lenstra, J. A. Mitchell, T. Sexton, Transcriptional regulation and chromatin architecture maintenance are decoupled functions at the *Sox2* locus. *Genes Dev.* **36**, 699–717 (2022).
21. T.-H. S. Hsieh, C. Cattoglio, E. Slobodyanyuk, A. S. Hansen, X. Darzacq, R. Tjian, Enhancer-promoter interactions and transcription are largely maintained upon acute loss of CTCF, cohesin, WAPL or YY1. *Nat. Genet.* **54**, 1919–1932 (2022).
22. S. Chakraborty, N. Kopitchinski, Z. Zuo, A. Eraso, P. Awasthi, R. Chari, A. Mitra, I. C. Tobias, S. D. Moorthy, R. K. Dale, J. A. Mitchell, T. J. Petros, P. P. Rocha, Enhancer-promoter interactions can bypass CTCF-mediated boundaries and contribute to phenotypic robustness. *Nat. Genet.* **55**, 280–290 (2023).
23. H. Saad, F. Gallardo, M. Dalvai, N. Tanguy-le-Gac, D. Lane, K. Bystricky, DNA dynamics during early double-strand break processing revealed by non-intrusive imaging of living cells. *PLOS Genet.* **10**, e100418 (2014).
24. H. Huang, Q. Zhu, A. Jussila, Y. Han, B. Bintu, C. Kern, M. Conte, Y. Zhang, S. Bianco, A. M. Chiariello, M. Yu, R. Hu, M. Tastemel, I. Juric, M. Hu, M. Nicodemi, X. Zhang, B. Ren, CTCF mediates dosage- and sequence-context-dependent transcriptional insulation by forming local chromatin domains. *Nat. Genet.* **53**, 1064–1074 (2021).
25. G. M. Oliveira, A. Oravecz, D. Kobi, M. Maroquenne, K. Bystricky, T. Sexton, N. Molina, Precise measurements of chromatin diffusion dynamics by modeling using Gaussian processes. *Nat. Commun.* **12**, 6184 (2021).
26. B. Bonev, N. M. Cohen, Q. Szabo, L. Fritsch, G. L. Papadopoulos, Y. Lubling, X. Xu, X. Lv, J. P. Hugnot, A. Tanay, G. Cavalli, Multiscale 3D genome rewiring during mouse neural development. *Cell* **171**, 557–572.e24 (2017).
27. E. de Wit, E. S. M. Vos, S. J. B. Holwerda, C. Valdes-Quezada, M. J. A. M. Verstegen, H. Teunissen, E. Splinter, P. J. Wijchers, P. H. L. Krijger, W. de Laat, CTCF binding polarity determines chromatin looping. *Mol. Cell* **60**, 676–684 (2015).
28. J. M. Alexander, J. Guan, B. Li, L. Maliskova, M. Song, Y. Shen, B. Huang, S. Lomvardas, O. D. Weiner, Live-cell imaging reveals enhancer-dependent *Sox2* transcription in the absence of enhancer proximity. *eLife* **8**, e41769 (2019).
29. S. Zhang, N. Übelmesser, M. Barbieri, A. Papantonis, Enhancer-promoter contact formation requires RNAPII and antagonizes loop extrusion. *Nat. Genet.* **55**, 832–840 (2023).
30. S. S. P. Rao, S. C. Huang, B. G. St Hilaire, J. M. Engreitz, E. M. Perez, K. R. Kieffer-Kwon, A. L. Sanborn, S. E. Johnstone, G. D. Bascom, I. D. Bochkov, X. Huang, M. S. Shamim, J. Shin, D. Turner, Z. Ye, A. D. Omer, J. T. Robinson, T. Schlick, B. E. Bernstein, R. Casellas, E. S. Lander, E. L. Aiden, Cohesin loss eliminates all loop domains. *Cell* **171**, 305–320.e24 (2017).
31. W. Schwarzer, N. Abdennur, A. Goloborodko, A. Pekowska, G. Fudenberg, Y. Loe-Mie, N. A. Fonseca, W. Huber, C. H. Haering, L. Mirny, F. Spitz, Two independent modes of chromatin organization revealed by cohesin removal. *Nature* **551**, 51–56 (2017).
32. E. J. Banigan, W. Tang, A. A. van den Berg, R. R. Stocsits, G. Wutz, H. B. Brandão, G. A. Busslinger, J. M. Peters, L. A. Mirny, Transcription shapes 3D chromatin organization by interacting with loop extrusion. *Proc. Natl. Acad. Sci. U.S.A.* **120**, e2210480120 (2023).
33. S. Chahar, Y. B. Zouari, H. Salari, D. Kobi, M. Maroquenne, C. Erb, A. M. Molitor, A. Mossler, N. Karasu, D. Jost, T. Sexton, Transcription induces context-dependent remodeling of chromatin architecture during differentiation. *PLOS Biol.* **21**, e3002424 (2023).
34. B. Lim, M. S. Levine, Enhancer-promoter communication: Hubs or loops? *Curr. Opin. Genet. Dev.* **67**, 5–9 (2021).
35. N. S. Benabdallah, I. Williamson, R. S. Illingworth, L. Kane, S. Boyle, D. Sengupta, G. R. Grimes, P. Therizols, W. A. Bickmore, Decreased enhancer-promoter proximity accompanying enhancer activation. *Mol. Cell* **76**, 473–484.e7 (2019).
36. I. I. Cissé, I. Izeddin, S. Z. Causse, L. Boudarene, A. Senecal, L. Muresan, C. Dugast-Darzacq, B. Hajj, M. Dahan, X. Darzacq, Real-time dynamics of RNA polymerase II clustering in live human cells. *Science* **341**, 664–667 (2013).
37. J. Li, A. Hsu, Y. Hua, G. Wang, L. Cheng, H. Ochiai, T. Yamamoto, A. Pertsinidis, Single-gene imaging links genome topology, promoter-enhancer communication and transcriptional control. *Nat. Struct. Mol. Biol.* **27**, 1032–1040 (2020).
38. B. Pradhan, R. Barth, E. Kim, I. F. Davidson, B. Bauer, T. van Laar, W. Yang, J. K. Ryu, J. van der Torre, J. M. Peters, C. Dekker, SMC complexes can traverse physical roadblocks bigger than their ring size. *Cell Rep.* **41**, 111491 (2022).

39. S. D. Moorthy, J. A. Mitchell, Generating CRISPR/Cas9 mediated monoallelic deletions to study enhancer function in mouse embryonic stem cells. *J. Vis. Exp.* **110**, e53552 (2016).
40. E. Tutucci, M. Vera, J. Biswas, J. Garcia, R. Parker, R. H. Singer, An improved MS2 system for accurate reporting of the mRNA life cycle. *Nat. Methods* **15**, 81–89 (2018).
41. J. Rodriguez, G. Ren, C. R. Day, K. Zhao, C. C. Chow, D. R. Larson, Intrinsic dynamics of a human gene reveal the basis of expression heterogeneity. *Cell* **176**, 213–226.e18 (2019).
42. H. Hajjoul, J. Mathon, H. Ranchon, I. Goiffon, J. Mozziconacci, B. Albert, P. Carrivain, J.-M. Victor, O. Gadal, K. Bystricky, A. Bancaud, High-throughput chromatin motion tracking in living yeast reveals the flexibility of the fiber throughout the genome. *Genome Res.* **23**, 1829–1838 (2013).
43. B. Langmead, C. Trapnell, M. Pop, S. L. Salzberg, Ultrafast and memory-efficient alignment of short DNA sequences to the human genome. *Genome Biol.* **10**, R25 (2009).
44. Y. Ben Zouari, A. Platania, A. M. Molitor, T. Sexton, 4See: A flexible browser to explore 4C data. *Front. Genet.* **10**, 1372 (2020).
45. G. Geeven, H. Teunissen, W. de Laat, E. de Wit, PeakC: A flexible, non-parametric peak calling package for 4C and Capture-C data. *Nucleic Acids Res.* **46**, e91 (2018).
46. M. E. Ritchie, B. Phipson, D. Wu, Y. Hu, C. W. Law, W. Shi, G. K. Smyth, *Limma* powers differential expression analyses for RNA-sequencing and microarray studies. *Nucleic Acids Res.* **43**, e47 (2015).
47. K. J. Meaburn, T. Misteli, Locus-specific and activity-independent gene repositioning during early tumorigenesis. *J. Cell Biol.* **180**, 39–50 (2008).
48. S. Kocanova, I. Goiffon, K. Bystricky, 3D FISH to analyse gene domain-specific chromatin re-modeling in human cancer cell lines. *Methods* **142**, 3–15 (2018).
49. A. Coulon, M. L. Ferguson, V. de Turris, M. Palangat, C. C. Chow, D. R. Larson, Kinetic competition during the transcription cycle results in stochastic RNA processing. *eLife* **3**, e03939 (2014).
50. F. de Chaumont, S. Dallongeville, N. Chenouard, N. Hervé, S. Pop, T. Provoost, V. Meas-Yedid, P. Pankajakshan, T. Lecomte, Y. Le Montagner, T. Lagache, A. Dufour, J.-C. Olivo-Marin, Icy: An open bioimage informatics platform for extended reproducible research. *Nat. Methods* **9**, 690–696 (2012).
51. N. Tarantino, J.-Y. Tinevez, E. F. Crowell, B. Boisson, R. Henriques, M. Mhlanga, F. Agou, A. Israël, E. Laplantine, TNF and IL-1 exhibit distinct ubiquitin requirements for inducing NEMO-IKK supramolecular structures. *J. Cell Biol.* **204**, 231–245 (2014).
52. U. Gowthaman, M. Ivanov, I. Schwarz, H. P. Patel, N. A. Müller, D. García-Pichardo, T. L. Lenstra, S. Marquardt, The Hda1 histone deacetylase limits divergent non-coding transcription and restricts transcription initiation frequency. *EMBO J.* **40**, e108903 (2021).
53. B. J. Reynwar, G. Illya, V. A. Harmandaris, M. M. Müller, K. Kremer, M. Deserno, Aggregation and vesiculation of membrane proteins by curvature-mediated interactions. *Nature* **447**, 461–464 (2007).
54. A. M. Chiariello, C. Annunziatella, S. Bianco, A. Esposito, M. Nicodemi, Polymer physics of chromosome large-scale 3D organisation. *Sci. Rep.* **6**, 29775 (2016).
55. A. Buckle, C. A. Brackley, S. Boyle, D. Marenduzzo, N. Gilbert, Polymer simulations of heteromorphic chromatin predict the 3D folding of complex genomic loci. *Mol. Cell* **72**, 786–797.e11 (2018).
56. M. Barbieri, S. Q. Xie, E. T. Triglia, A. M. Chiariello, S. Bianco, I. de Santiago, M. R. Branco, D. Rueda, M. Nicodemi, A. Pombo, Active and poised promoter states drive folding of the extended HoxB locus in mouse embryonic stem cells. *Nat. Struct. Mol. Biol.* **24**, 515–524 (2018).
57. K. Kruse, C. B. Hug, J. M. Vaquerizas, FAN-C: A feature-rich framework for the analysis and visualisation of chromosome conformation capture data. *Genome Biol.* **21**, 303 (2020).
58. M. Sánchez-Castillo, D. Ruau, A. C. Wilkinson, F. S. L. Ng, R. Hannah, E. Diamanti, P. Lombard, N. K. Wilson, B. Gottgens, CODEX: A next-generation sequencing experiment database for the haematopoietic and embryonic stem cell communities. *Nucleic Acids Res.* **43**, D1117–D1123 (2015).


**Acknowledgments:** We thank P. Mach, P. Kos, and L. Giorgetti for sharing data tracking transgenic lacO/TetO reporters. ANCHOR constructs were provided by NeoVirTech. The MS2v6 constructs were built by B. Atanasovska. Sequencing was performed by the Institute of Genetics and Molecular and Cellular Biology (IGBMC) GenomEast platform, a member of the France Génomique consortium (ANR-10-INBS-0009). This study was made possible by the IGBMC Imaging Center flow cytometry and molecular biology platforms. BioRender was used for generating Figs. 3A and 4G. **Funding:** This work was supported by the following: European Research Council Starting grant 678624, CHROMTOPOLOGY (T.S.); LabEx INRT (ANR-10-LABX-0030-INRT, a French State fund managed by the Agence Nationale de la Recherche under the frame program Investissements d'Avenir ANR-10-IDEX-0002-02) (T.S.); Agence Nationale de Recherche HUBDYN (T.S.); Ligue Nationale Contre le Cancer (A. Pl.); University of Strasbourg Institute of Advanced Study (T.S. and M.N.); Canadian Institute of Health Research FRN PJT153186 and PJT180312 (J.A.M.); National Institute of Health R01-HG010045-01 (J.A.M.); Canada Foundation for Innovation (J.A.M.); Ontario Ministry of Research and Innovation (J.A.M.); Natural Sciences and Engineering Research Council of Canada (V.M.S.); Academy of Medical Sciences (E.S.); Dutch Cancer Society (T.L.L.); Dutch Ministry of Health, Welfare, and Sport (T.L.L.); Oncode Institute, partly financed by the Dutch Cancer Society (T.L.L.); Deutsche Forschungsgemeinschaft via the SPP2191 and SPP2202 Priority Programs (project nos. PA 2456/17-1 and PA 2456/11-2) (A. Pa); Agence Nationale de Recherche SINFONIE (K.B.); and Fondation ARC (K.B.). **Author contributions:** Conceptualization: T.S., A. Pl., and K.B. Methodology: A. Pl., C.E., M.B., B.M., E.G., M.A.C.d.K., K.M., T.T., V.M.S., S.K., M.N., G.M.O., and W.P. Investigation: A. Pl., C.E., M.B., B.M., E.G., M.A.C.d.K., K.M., T.T., V.M.S., S.K., M.N., G.M.O., W.P., N.M., A. Pa., and T.S. Funding acquisition: T.S., A. Pl., J.A.M., E.S., T.L.L., A. Pa., N.M., and K.B. Supervision: T.S., J.A.M., E.S., T.L.L., A. Pa., N.M., and K.B. Writing—original draft: A. Pl., C.E., M.B., B.M., E.G., M.A.C.d.K., K.M., T.T., V.M.S., S.K., M.N., G.M.O., E.S., J.A.M., T.L.L., A. Pa., N.M., K.B., and T.S. **Competing interests:** The authors declare that they have no competing interests. **Data and materials availability:** 4C-seq data have been deposited on the Gene Expression Omnibus with accession number GSE230243. All data needed to evaluate the conclusions in the paper are present in the paper and/or the Supplementary Materials. The ANCHOR system can be provided by NeoVirTech SAS pending scientific review and a completed material transfer agreement. Requests for the system should be submitted to: contact@neovirtech.com.

Submitted 26 April 2024
Accepted 7 November 2024
Published 13 December 2024
10.1126/sciadv.adq0987